UNIVERSITY of CALIFORNIA
SANTA CRUZ

A PATHWAY FOR COLLISIONAL PLANETESIMAL GROWTH IN THE ICE DOMINANT REGION OF PROTOPLANETARY DISKS

A thesis submitted in partial satisfaction of the
requirements for the degree of

BACHELOR OF SCIENCE

in

ASTROPHYSICS

by

Elizabeth Yunerman

6 June 2021

The thesis of Elizabeth Yunerman is approved by:

Professor Ruth Murray-Clay
Advisor

Professor Bruce Schumm
Chair, Department of Physics

Abstract

A Pathway for Collisional Planetesimal Growth in the Ice Dominant Region of Protoplanetary Disks

by

Elizabeth Yunerman

The "meter-size barrier" of planet formation has been one of the most persistent problems in formation models and our overall understanding of early stages of planet formation and evolution. Models demonstrate that once the dust and gas in a planet-forming disk coagulate into roughly meter-size boulders, growth completely halts and gravity is not sufficient to maintain the structural integrity of the boulders; instead, almost all grains begin to break apart from collisions or rapidly inspiral into their host-star. Previous studies of centimeter- to meter-size grain evolution fail to model the full parameter space necessary to capture the growth, inward drift, and fragmentation processes of these grains. We created an analytic model of these processes and consider all the relevant drag forces, material compositions, and most up-to-date observed protoplanetary disk properties and iceline calculations. The model's flexibility allows tests of grain stability and motion across an extremely broad parameter space, including where dust and ice grains will break apart due to collisions as a function of particle size, strength, composition, and distance from the host-star. We find that for certain grain compositions, fragmentation may not be a dominating factor and can potentially allow particles to grow to very large sizes, overcoming the meter-size barrier.

Contents

List of Figures

List of Tables

For the people who believed in me and the loved ones who passed.

Acknowledgements

I would like to thank Professor Ruth Murray-Clay and Dr. Diana Powell for providing me the foundation, encouragement, and support I needed to achieve my dreams and grow as a person and scientist. Their kind mentorship has changed my life for the better and I will always be grateful for the effort they put into nurturing me academically. I would also like to thank Professor Phil Hopkins and Dr. Jonathan Squire for giving me the opportunity to learn new methods of studying planet formation and evolution. Their support and guidance during the pandemic was extremely helpful and validating when I needed it the most. I thank Zafar Rustamkulov for uplifting me and sticking by my side during difficult times, and for celebrating the joys of life with me during wondrous times. I thank Dinara Tassin and Marilyn Patton for believing in me, and Professors Natalie Batalha, Nicole Feldl, Brant Robertson, Jonathan Fortney, Ian Garrick-Bethell, Xi Zhang, and Myriam Telus for getting me excited about astrophysics and planetary science. Thank you to my parents, Liliya and Igor Yunerman, for supporting me, loving me, and encouraging me to always try my best and be kind. Thank you to my brother, Alex, and my sister-in-law, Traci, for giving me the confidence and motivation to never give up even when things seem impossibly hard. Thank you to my best friend, Kuzya. Lastly, I'd like to thank Genrich Gilman for taking pride in me, Yevgeniya Lazhechnikova for always being compassionate to me, Polina Yunerman for taking care of me, and Marina Tsesina for being my sunshine.

1

Introduction

Planet formation begins immediately after a star is born. The left over gaseous dusty nebula collapses down into a rotating planet forming, or protoplanetary, disk in order to conserve angular momentum. Dust particles must then come together and grow from micron sizes all the way to planetary scales, however, the processes that lead to the growth of these particles across orders of magnitude in scale are still an active area of research in planet formation theory (Armitage, 2017). The classical problem arises due to the likelihood that particles will have to overcome several barriers to their continued growth before reaching sizes that can maintain their orbital and structural integrity and grow to planetary masses. Creating planetary building blocks, generally known as planetesimals, of kilometer sizes proves to be difficult in models and in theories. This is the "meter-size barrier" that results in millimeter- to meter-size particles either drifting towards their host-star significantly due to the particularly strong gas drag, or being destroyed due to collisional fragmentation which occurs when the relative velocities between particles are such that growth via coagulation can no longer occur (Weidenschilling, 1977b; Youdin, 2004; Youdin & Goodman, 2005; Blum

& Wurm, 2008). Once grains overcome this size barrier, other growth mechanisms take over and are able to produce planets and planetary systems. Figure 1.1 is an illustration of our general understanding of protoplanetary disk evolution and planet formation.

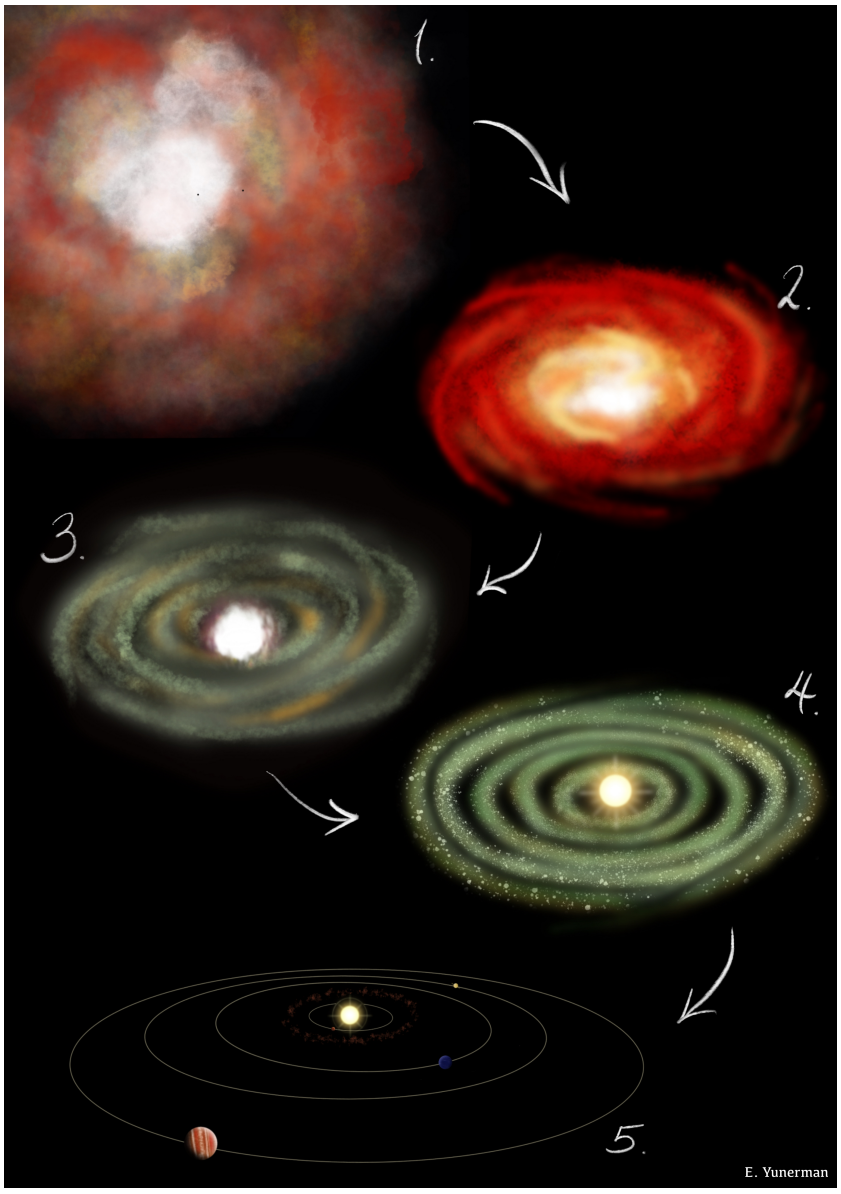

Figure 1.1: Overview of different stages of protoplanetary disk evolution and planet formation. Stage 1 is the leftover star forming nebular gas and dust. At stage 2, the molecular cloud collapses into a hot, rotating disk, and after some time the disk begins to cool down with some density structures emerging in stage 3. At stage 4, large disk structures form as a result of disk instabilities or planets beginning to carve out material as they orbit their host-star. After billions of years, at stage 5, a stable planetary system is left.

Several theories have been developed attempting to surpass the meter-size barrier. Youdin & Goodman (2005) demonstrated that the gaseous protoplanetary disk environment is unstable to the streaming instability, and as a result can clump dust into high density regions. Dust over-densities become unstable to the fluid instabilities and can then directly collapse under their own self-gravity into km-sized planetesimals (Goldreich & Ward, 1973; Youdin & Shu, 2002; Johansen et al., 2006; Chiang & Youdin, 2010; Simon et al., 2016). More recently, Squire & Hopkins (2018) found that several Resonant Drag Instabilities (RDIs), one of which being the streaming instability, can all play a significant role in seeding planetesimal formation. While formation through unstable RDIs is promising in overcoming the fragmentation barrier, these models rely on strict initial conditions that do not yet represent the diversity of disk conditions that exist and can only produce large planetesimals. A separate approach has looked at how micron-sized icy dust aggregates stick together forming fluffy planetesimals and are able to surpass the drift barrier without fully fragmenting (Kataoka et al., 2013). Similarly, Wada et al. (2007, 2009) numerically modeled how different icy dust aggregates are able to retain material during various collisions of ranging impact parameters and velocities. While all of these studies have made significant progress in understanding the underlying problem, they all make strict, simplifying assumptions and approximations that exclude important governing physics.

The process of fragmentation depends sensitively on assumptions regarding the background disk conditions (i.e. the total disk mass), the abundance of particles, and the particles' material properties. Previous work on the physics of fragmentation in protoplanetary disks has primarily consisted of laboratory experiments, or has focused on the interpretation of laboratory and numerical computation experiments. Specifically, fragmentation of

similarly sized particles from the millimeter to sub-kilometer sizes was demonstrated in Blum & Wurm (2008). Stewart & Leinhardt (2009) studied fragmentation of solid and somewhat porous rocks ranging in mass over many orders of magnitude and up-to gravitationally held planetesimals. Modeling fragmentation in terms of critical fragmentation surface energies allowed calculations of critical fragmentation velocities. Similarly, but studying centimeter-sized water-ice particles composed of micron-sized monomers, Wada et al. (2007, 2009) were able to calculate the critical fragmentation velocity to break off monomers. Our model compares the relative velocities of particles in protoplanetary disks of various composition and size with the critical fragmentation velocities from these studies. We also recalculate and expand the critical velocity study from Wada et al. (2007, 2009) to include up-to-date H_2O, CO, CO_2, SiO_2, and $MgSiO_4$ molecular properties. H_2O, CO, and CO_2 are ices expected to be found in mid to outer regions of the disk, while SiO_2 and Mg_2SiO_4 are silicates expected throughout the disk.

In this work, we study the material and disk properties that are likely to control the process of fragmentation in order to investigate the likelihood whether fragmentation is a significant barrier to particle growth. We identify the properties of solid material that merit further study both in laboratory experiments and observational surveys. In addition to the particle size, we focus our study on several key material properties that determine the onset of collisional disruption: the particle composition and aggregate strengths. In cases where we assume standard monomer sizes and particle compositions, we find that neither fragmentation nor particle drift impose a barrier to particle growth throughout large swaths of disk orbital distances.

2

Critical Velocity for Collisional Destruction

Collisions of roughly meter-size grains can be thought of in two separate but equally important ways. For solid rocks, with very minimal porosity, fragmentation can happen along the weakest point. Ultimately, a crack can significantly weaken a solid rock for it to easily fragment. For porous rocks or aggregates, each connection making up the full aggregate must be broken since collisions between porous grains tend to compact an aggregate as opposed to fully break them apart. Whether the governing process is either solid-rock or aggregate fragmentation is still unclear.

Experimental and numerical work have helped to better understand which kind of collisions of like-sized particles will fragment. Figure. 2.1 is a summary created by Blum & Wurm (2008) that puts together multiple experimental studies of particle-particle collision coupled with numerical calculations of the collision velocities for the minimum mass solar nebula (MMSN, detailed discussion in §3.1.1) (Blum et al., 1998, 2000, 2002; Wurm & Blum,

1998; Krause & Blum, 2004; Dominik & Tielens, 1997; Blum & Wurm, 2000; Wada et al., 2007; Blum & Münch, 1993; Wurm et al., 2005; Schäfer et al., 2007; Blum & Schräpler, 2004; Blum et al., 2006; Langkowski et al., 2008; Paraskov et al., 2007)). Once the two colliding particles enter the roughly meter-size region of the figure, all collisions result in mass loss, meaning they are fully fragmenting.

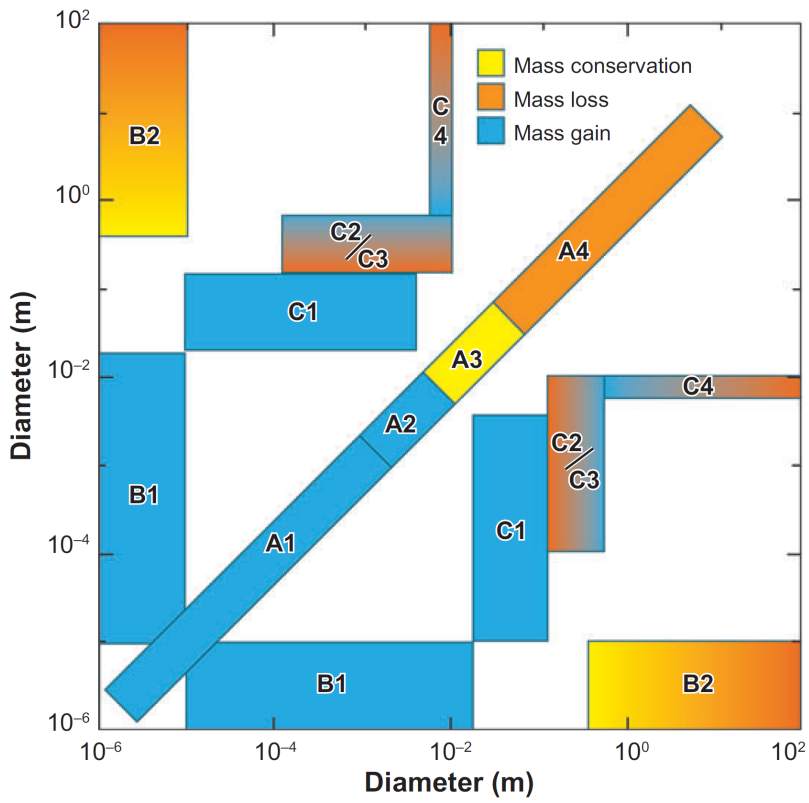

Figure 2.1: Figure 12 from Blum & Wurm (2008). The axes represent each colliding particle, the boxes are different experiments and the size range they study. The experiments in blue have resulted in collisional growth, while the experiments in orange have resulted in collisional destruction. The small regions of yellow had a system of mass conservation where the two particles bounced off of each other and did not gain or lose any mass.

.

This chapter will derive and expand on the critical fragmentation velocity studies of Stewart & Leinhardt (2009) in §2.1 and of Wada et al. (2007, 2009) in §2.2. The material

properties governing these collisions throughout protoplanetary disks and their significance to this study will be discussed in §2.3.

2.1 Fragmentation of Solid and Porous Bodies

Stewart & Leinhardt (2009) define a fragmentation criterion as the disruption energy per mass for planetesimals ranging in strength dominated bodies and in gravity dominated bodies.

$$Q^*_{RD} = \left(q_s R_{C1}^{9\mu/(3-2\phi)} + q_g R_{C1}^{3\mu}\right) V_i^{2-3\mu} \tag{2.1}$$

The term on the left, $q_s R_{C1}^{9\mu/(3-2\phi)}$, represents the strength regime (small particles bonded together), while the term on right, $q_g R_{C1}^{3\mu}$, represents the gravity regime (rubble piles gravitationally held together). Here q_s, q_g, μ, and ϕ (this ϕ is not the grain porosity discussed in §4.3) define the material properties and are all in cgs units. The material values are presented in Stewart & Leinhardt (2009) and the ones used in this study can be found in table 2.1. R_{C1} is the combined projectile and target spherical radius of density 1 g cm^{-3}. For our purposes we approximate R_{C1} as the target size and the disruption criterion for our target sizes is not expected to be dominated by the gravity regime. Figure 2.2 demonstrates how the disruption criterion changes as a function of target size and collision velocity, V_i. Several experimental points of basalt and porous glass are shown as a reference for what some protoplanetary disk materials may resemble.

Table 2.1: Fragmentation Criterion Material Properties (Stewart & Leinhardt, 2009)

Rock Type	q_s	q_g	μ	ϕ
Strong Rock	7×10^4	10^{-4}	0.5	8
Weak Rock	500	10^{-4}	0.4	7

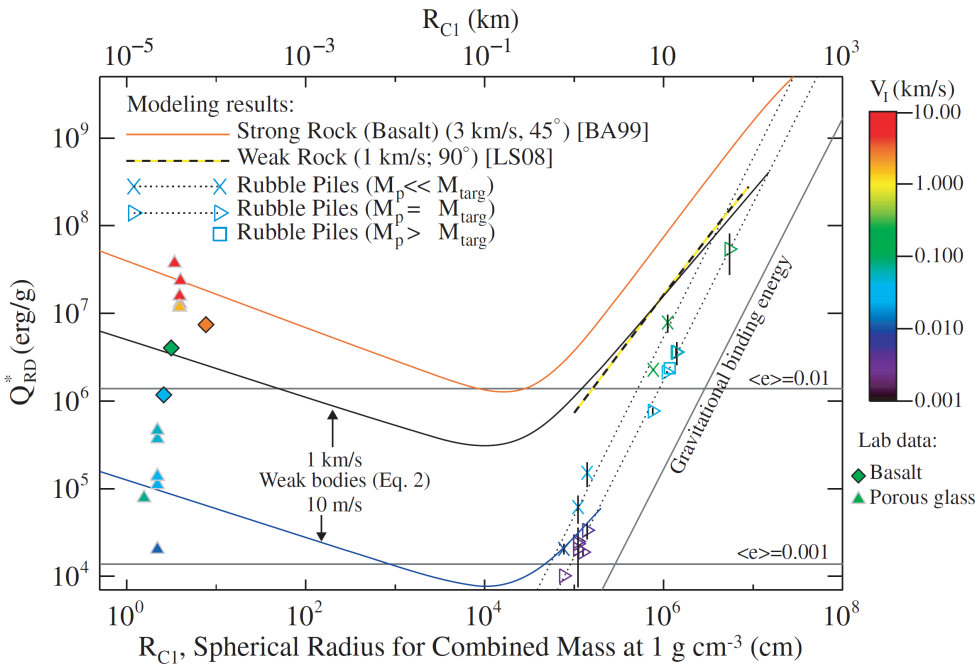

Figure 2.2: Figure 2 from Stewart & Leinhardt (2009). Each curve is the disruption criterion compared to the target size for different rock strengths. The diamond points (basalt) and the triangle points (porous glass) represent experimental values at various collisional velocities denoted by their color.

.

The above disruption criterion can be used as the binding energy keeping together the either compact or porous rubble pile. Comparing this energy with the collisional kinetic energy of a projectile provides the critical velocity needed to break apart or make cracks in the target. Here the kinetic energy of the projectile is simply $KE = (1/2)m_{\rm p}v_{\rm rel}^2$, while the binding energy of the target particle is $BE = m_{\rm t}Q^*_{RD}$, where $m_{\rm p}$ and $m_{\rm t}$ are the masses of the projectile and target respectively. Converting the masses in terms of the target radius, R_{C1}, and solving for the relative velocity $v_{\rm rel}$, we find that the critical velocity required to break apart the target is

$$v_{crit} = \sqrt{\frac{2}{f^3}Q^*_{RD}} \tag{2.2}$$

where f is the size ratio between the projectile radius and the target radius. In this study we take the size ratio to be 0.5, where the the collision occurs between a particle and one that is half its size.

2.2 Fragmentation of Icy Aggregates

We follow the work of Wada et al. (2007) and Wada et al. (2009) to find the critical velocity of water ice aggregate collisions. Their numerical studies modeled the collisions between ballistic cluster-cluster aggregation (BCCA) and ballistic particle-cluster aggregation (BPCA), or more generally fluffy and compact aggregates. Figure 2.3 is a visual representation of these aggregates.

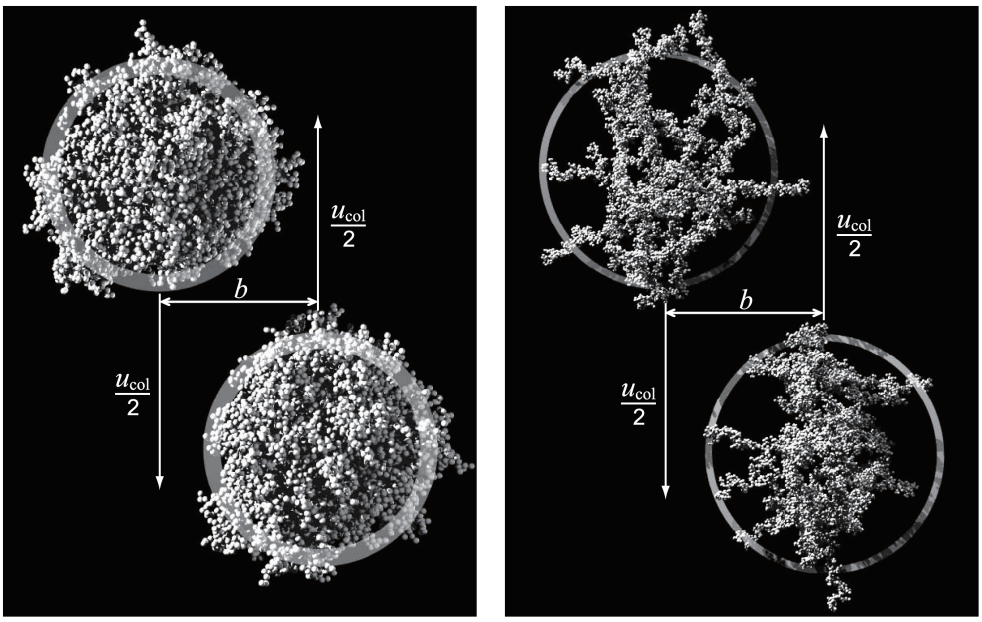

Figure 2.3: Figure 1 from Wada et al. (2009). The left panel is the visual for a collision between BPCA aggregates and the right panel is the visual for a collision between BCCA aggregates. b is the impact parameter between the two particles and u_{col} is the velocity of the particles upon impact.

.

This kind of fragmentation focuses on pulling apart each monomer, as opposed to in the solid fragmentation from §2.1. The energy required to break apart two contact monomers is

$$E_{\text{break}} = 1.54 F_{\text{c}} \delta_{\text{c}} \tag{2.3}$$

with

$$\begin{aligned} F_{\text{c}} &= 3\pi\gamma R, \\ \delta_{\text{c}} &= (9/16)^{1/3} a_0^2/(3R) \end{aligned} \tag{2.4}$$

F_{c} is the maximum force required to separate the contact and δ_{c} is the critical separation or compression distance between the monomers. These expressions depend on the contact circle radius $a_0 = (9\pi\gamma R/E^*)^{2/3}$ (Wada et al., 2007), $1/R = 1/r_1 + 1/r_2$ with r_1 and r_2 being the monomer radii, and $1/E^* = (1-\nu_1^2)/E_1 + (1-\nu_2^2)/E_2$ (Wada et al., 2009). All of these are a function of the material properties, Young's modulus (E), Poisson's ratio (ν), surface energy (γ), and the material density (ρ), further discussed in §2.3.

The kinetic energy of a colliding aggregate is $KE = (1/2)N_{\text{total}} m (v_{\text{rel}}/2)^2$, where N_{total} is the total number of particles between both aggregates and $m = (4/3)\pi r^3 \rho$ is the mass of a monomer. The critical impact energy is $E_{\text{crit}} = k N_{\text{total}} E_{\text{break}}$, where k is a dimensionless factor which takes into account whether the aggregate is fluffy or compact. Wada et al. (2009) find that for fluffy aggregates (BCCA) $k \sim 10$, while for compact aggregates (BPCA) $k \sim 30$. The critical relative velocity is then found by balancing the kinetic energy with the critical impact energy and solving.

$$v_{\text{crit}} = \sqrt{\frac{8kE_{\text{break}}}{m}} \tag{2.5}$$

2.3 Material Properties Governing Collisions

The material properties of a given species determines the likelihood of collisional disruption. In the case of aggregate particles these properties are: the monomer size, the species' surface energy, Young's modulus, Poisson's ratio, and material density. The species specific material properties are given in Table 2.2. Values in the table for SiO_2 and H_2O are from Shivamurthy et al. (2019), and in brackets from Wada et al. (2009). Mg_2SiO_4 values are from Kozasa et al. (1989) and Gaillac et al. (2016), CO_2 values are from Mazzoldi et al. (2008) and Musiolik & Wurm (2019), and CO values are from Sprow & Prausnitz (1966) and its Poisson's ratio is approximated by the CO_2 value.

Table 2.2: Species Material Properties

Species	Surface Energy [erg cm^{-2}]	Young's Modulus [GPa]	Poisson's Ratio	Material Density [g cm^{-2}]
H_2O	72.8 [100]	7	0.25	1
CO	23.1	1.5	0.544	0.789
CO_2	170	13.12	0.544	1.56
SiO_2	62.7 [25]	54	0.17	2.65
Mg_2SiO_4	436	187.05	0.24259	3.21

The monomer size of the aggregate particles is unconstrained; however, a common choice of size is 0.1 μm (Blum & Wurm, 2008) which corresponds to the typical size of a grain in the interstellar medium. We detail below three physically-motivated cases that may occur in protoplanetary disks and lead to significantly different predictions for the size in which particles fragment. These cases correspond to particles that have fragmentation properties that resemble those of: (1) an ice-coated aggregate comprised of small monomers, (2) an ice-coated aggregate comprised of large monomers, and (3) an ice-coated compact particle. A corollary potential case of an aggregate particle behaving like an ice-free aggregate composed

of small monomers is also discussed.

Initially, the small monomers present in the disk will grow via coagulation and form larger, potentially aggregate, particles. We expect that the monomers and smaller aggregates will be largely ice-free due to their small surface areas which will inhibit the stable nucleation of volatile species due to the effect of surface tension (i.e., the Kelvin effect, Powell et al., 2020). Eventually, a fraction of these aggregate particles will grow to a size large enough for a stable coating of ice to form (Powell et al., 2020) as shown in Figure 2.4. After particles reach the critical size for ice formation, the pathway to further growth is unclear and likely depends on the current evolutionary stage of the system.

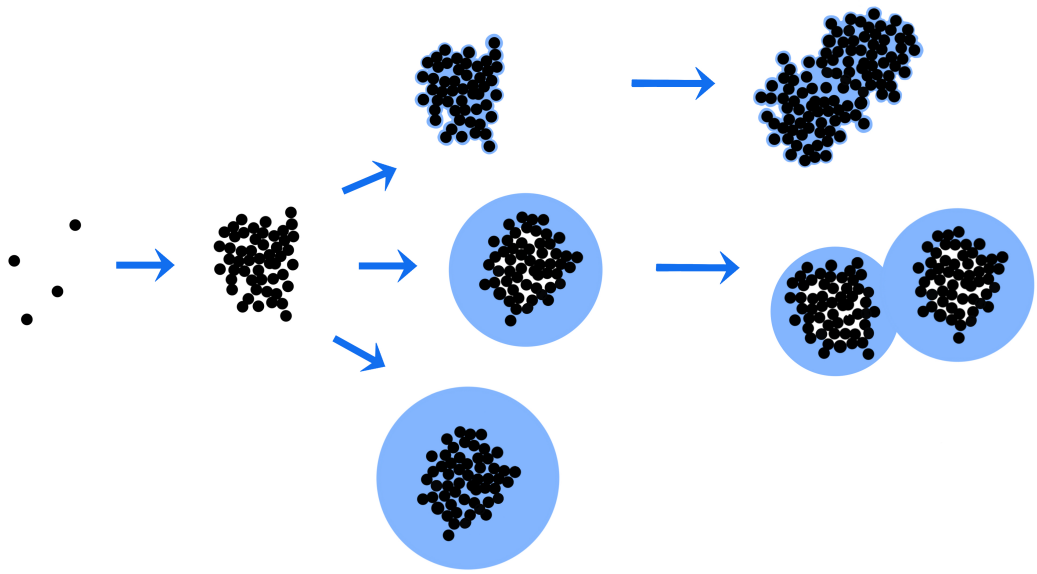

Figure 2.4: Visual representation of the three ice coating growth scenarios. At first, the monomers stick together via the Kelvin effect and if the aggregate is in a region of the disk where ice (blue) does not sublimate, then three cases can occur. The aggregate and monomer connections are either covered completely in a thin layer of ice, the aggregate is covered largely by ice while the monomer connections are not, and lastly, the aggregate and the monomer connections are covered largely by ice.

.

Case 1: In the first potential case, a small coating of ice covers the entirety of the aggregate particle, including the surface of the grain and in the cavities of the aggregate particle. This scenario is likely to occur when there is a sufficient number of large particles that quickly deplete the available supply of volatile gas. Once ice forms on the abundant large aggregates, further particle growth will be dominated by coagulation of ice-coated aggregates with similar properties(i.e., particle size, Birnstiel et al., 2012). The resultant large particles that are produced via this growth scenario will then resemble an aggregate particle comprised of 0.1 μm sized monomers where the connections between the grains are dominated by the material properties of the dominant ice species coating the surface.

Case 2: In the second potential case, a large coating of ice will cover the surface of the grains. This scenario is likely to occur if there is a more abundant supply of volatile gas than in Case 1 but there still exists a large number of sufficiently large aggregates that have become ice-coated. In this case, once the particles have depleted the available supply of volatile gas, further particle growth will be dominated by collisions with particles of similar sizes. Due to the large coating of ice on each particle, these collisions leading to particle growth may produce particles with fragmentation properties similar to those of an ice-coated aggregate with large-size monomers.

Case 3: In the third potential case, ice will form at a very efficient rate and will quickly dominate the particles properties. This scenario is likely to occur if volatile gas is abundant and there is a limited supply of large particles. In this case, the limited number of large particles will abundantly form ice and are unlikely to grow further via coagulation due to their low relative number densities. The fragmentation properties of these particles are likely to resemble that of a compact icy grain and not those of an aggregate particle.

In the ice free case, the connections between the monomers are dominated by the material properties of the ice-free monomer cores which are likely composed of grains that are silicate in composition. This case is likely for small particles and may also occur if ice formation is inefficient or the volatile gas supply is depleted. The ice free case is most likely important for silicate grains in the inner disk where all ices sublimate.

These different cases will lead to particles with different critical fragmentation velocities as shown in Figure 2.5. Particles with large monomers will fragment at significantly lower velocities than those with smaller monomers, meaning they are much easier to fragment. The fragmentation velocities for the ices comprised of 0.1 μm monomers are comparable to the strong rock from §2.1, while 1 μm monomers are comparable to the weak rock from §2.1.

In addition to the monomer size, the likelihood of fragmentation depends on the material properties listed in Table 2.2. These properties determine $E_{\rm break}$ as described in §2.2. In our modeling, we discuss the fragmentation of key volatiles in the disks including H_2O, CO, and CO_2, as well as two rock species that are only volatile in the very innermost high temperature regions of the disk. While previous studies have frequently focused on the fragmentation of SiO_2, we note that in comets the majority of non-volatile solid material has a composition similar to that of Mg_2SiO_4. We thus consider the fragmentation properties of both of these species. A BCCA aggregate comprised of SiO_2 is the weakest material, while a BPCA aggregate comprised of CO_2 ice is the strongest material and is thought to be common in the outer disk.

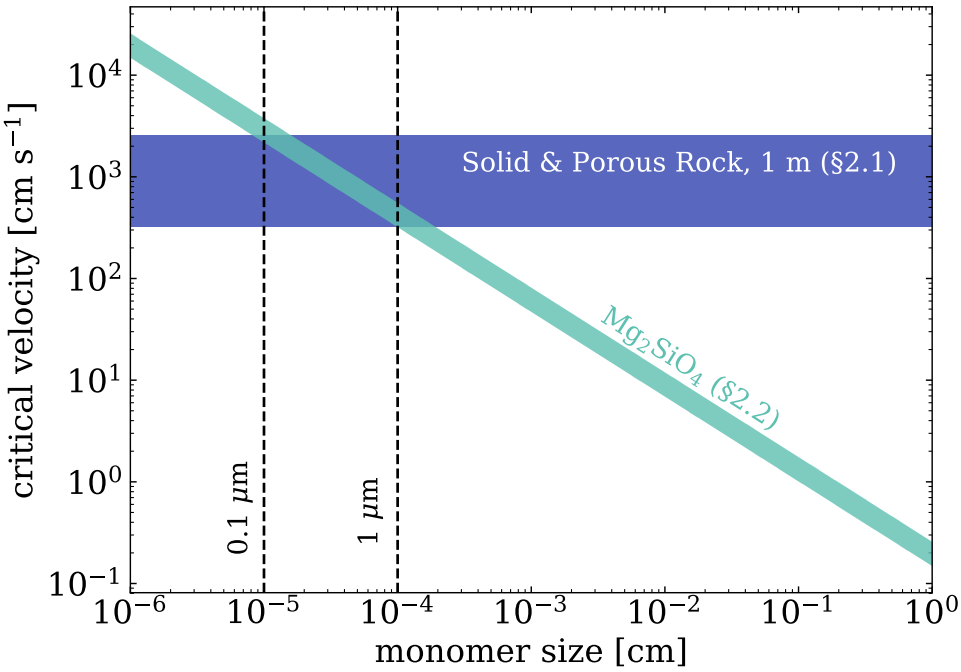

Figure 2.5: The critical velocity of aggregates for all compositions strongly depends on the monomer size which remains fairly unconstrained. Regions of aggregate fragmentation are bounded by BCCA and BPCA aggregates from Wada et al. (2009). Mg_2SiO_4 demonstrates this strong monomer size dependence, however all compositions in this study have the same behaviour. Their study solely focuses on 0.1 micron monomers. The Solid & Porous Rock region is the fragmentation critical velocity for a meter-sized rock following the Stewart & Leinhardt (2009) energy calculations. The porous rock defines the lower bound as it can be destroyed by lower impact velocities, while the solid rock can withstand higher velocities defining the upper bound.

.

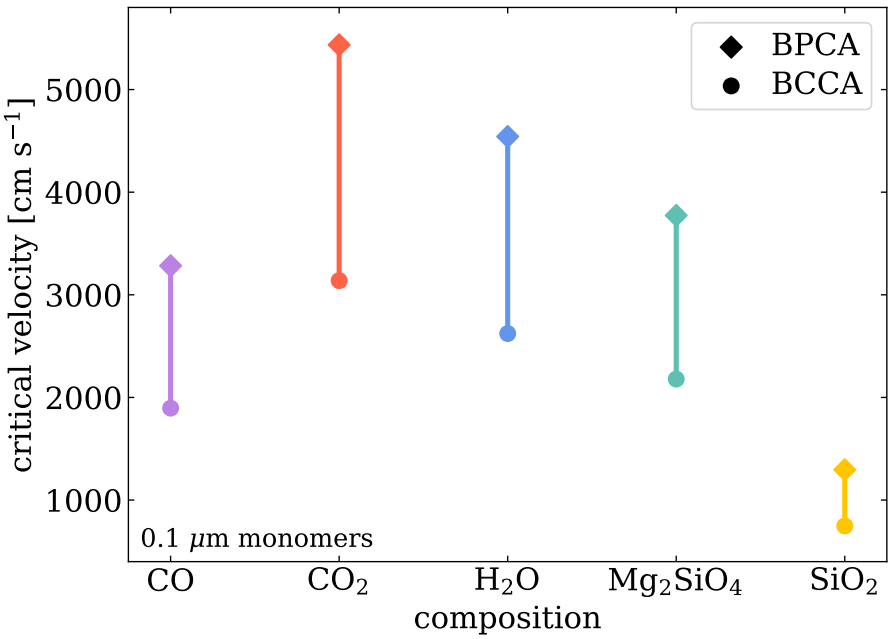

Figure 2.6: Different aggregate compositions and porosity levels define the overall strength of particles. Compact CO_2 ice is the strongest aggregate while SiO_2 is the weakest aggregate. Mg_2SiO_4 is the expected composition for the majority of particles in protoplanetary disks. Although Mg_2SiO_4 is relatively weaker than other compositions it likely has a coating of stronger ice in the outer regions of the disk increasing its ability to withstand higher impact velocities.

.

3

Protoplanetary Disk Parameters

The first component of our model is to use properties of observed disks to gain a better intuition for the environment these dynamic grains are in, including temperature and surface density profiles, as well as molecular species icelines. Disk properties are crucial initial conditions of modeling planet formation and evolution. Previous studies have relied on using the minimum mass solar nebula (MMSN) as a lower bound approximation of the amount of material needed to form the planets in the solar system (Hayashi, 1981). Extrapolating from this result, an analysis of the minimum mass extrasolar nebula (MMEN) was derived to be five times more massive than the MMSN (Chiang & Laughlin, 2013), and recent observational and theoretical studies of protoplanetary disks indicate that the observed disk masses are much higher than previously assumed. Observational studies infer the disk mass using dust and carbon monoxide mass tracers to estimate the mass. However, the main constituent of protoplanetary disks is molecular hydrogen, which is inaccessible to observations. Without viable observations of the main mass constituent, the inferred disk mass can be erroneously lower by orders of magnitude (e.g. Pollack et al., 1996; Vorobyov,

2011; Bergin et al., 2013; Powell et al., 2017, 2019). Thus, in our modeling we use updated and derived surface densities from Powell et al. (2019), which reflect a larger mass than the MMSN, to initialize our models.

3.1 Temperature & Surface Density Profiles

Table 3.1: Protoplanetary Disk Properties (Powell et al., 2019)

Disk	Stellar Mass [$M\odot$]	Stellar Luminosity [$L\odot$]	T_o [K]	Σ_o [g cm^{-2}]	r_c [AU]	γ
MMSN	1.0	1.0	210	-	-	-
TW Hya	0.8	0.28	82	175	30	1
HD 163296	2.3	36	284	29	213	0.39
DR Tau	0.8	1.09	121	315	20	1.07
CY Tau	0.48	0.4	98	55	65.6	0.28
AS 209	0.9	1.5	131	44	98	0.91
FT Tau	0.55	0.31	89	183	28	1.07
DoAr 25	1.0	1.3	123	68	105	0.36

3.1.1 MMSN

While the MMSN is a lower bound to protoplanetary disk masses, it can still be used as a point of comparison to some of the protoplanetary disks that have been observed. Weidenschilling (1977b) and Hayashi (1981) derive the surface density profile for the MMSN as

$$\Sigma_{\mathrm{MMSN}} = 1700 \text{ g cm}^{-2} \times r_{\mathrm{AU}}^{-3/2} \tag{3.1}$$

where r is the orbital radius in AU. Solar mass and luminosity are used for the MMSN profile. The temperature profile follows the same profile as for observed disks.

3.1.2 Observed Disks

The model is able to derive the fragmentation regions for all disks mentioned in table 3.1. TW Hya is used as the primary example and is compared to the MMSN, however the final result for the other disks will be included in future work. The surface density profile for the observed disks, comes from the self-similar solution to the viscous equations and is prescribed by Powell et al. (2019) as

$$\Sigma = \Sigma_o \left(\frac{r}{r_\mathrm{c}}\right)^{-\gamma} \exp\left[-\left(\frac{r}{r_\mathrm{c}}\right)^{2-\gamma}\right] \tag{3.2}$$

where Σ_o is the derived surface density constant, r_c is the critical radius, and γ is the power law parameter (e.g. Lynden-Bell & Pringle, 1974; Hartmann et al., 1998). Values for Σ_o, r_c, and γ can be found in table 3.1.

Protoplanetary disks are defined as either passive or active depending on their heat source. In a passive disk, stellar irradiation is the dominant heat source for the entire disk, and will cause the disk to absorb incoming radiation from the host star in local regions and re-emit it as a blackbody. An active disk includes viscous heating caused by accretion of the disk onto the host-star. Viscous heating is only dominant in the inner disk and will push the H_2O iceline, the boundary where water ice is stable, further out in the disk. Irradiation heating will always be the dominant heat source in the mid to outer disk (Armitage, 2017).

The irradiation temperature is

$$T_\mathrm{irradiation} = T_o r^{-3/7} \tag{3.3}$$

where

$$T_o = \left(\frac{2}{7}\right)^{1/4} \left(\frac{L_*}{4\sigma_\mathrm{SB}\pi}\right)^{2/7} \left(\frac{k}{\mu G M_*}\right)^{1/7} r^{-3/7} \tag{3.4}$$

L_* and M_* are the stellar luminosity and mass, $\sigma_{\rm SB}$ is the Stefan-Boltzmann constant, k is the Boltzmann constant, G is Newton's gravitational constant, and $\mu = 2.3m_{\rm H}$ is the reduced mass assuming a hydrogen-helium composition. Calculated values of T_o at a semi-major axis of 1 AU for our disks can be found in table 3.1.

The temperature due to viscous heating is

$$T^4_{\rm accretion} = \frac{9}{32\pi}\frac{\tau_{\rm vert}}{\sigma_{\rm SB}}\dot{M}\Omega^2 \tag{3.5}$$

$\tau_{\rm vert} = 0.5\Sigma\kappa$ is the vertical optical depth in the disk, where κ is the opacity and Σ is the disk surface density. We use $\kappa = 0.5$ cm^2 g^{-1} and a standard observed mass accretion rate, $\dot{M} = 10^8 M_\odot/yr$. Ω is the orbital frequency. For our modeling purposes the turbulence parameter α, how turbulent the disk is, is the same value when calculating the viscous heating and the relative velocity between the particles, although in general, they do not need to be equal.

For an active disk, we combine the irradiation and accretion temperatures as such:

$$T_{\rm total} = (T^4_{\rm irradiation} + T^4_{\rm accretion})^{1/4} \tag{3.6}$$

3.2 Icelines

Disk icelines are where molecules will freeze out depending on their adsorption and desorption fluxes. Without viscous heating, passive disks have icelines that are closer in towards their host star. When we calculate where fragmentation occurs based off of composition, ices will dominate the strength of particles beyond their respective icelines, changing the regions of fragmentation. In our work, we will consider the H_2O, CO_2, and CO icelines which are common volatiles used when studying protoplanetary disk chemistry.

Icelines are found by balancing the adsorption and desorption fluxes (Hollenbach et al., 2008; Öberg et al., 2011; Powell et al., 2017):

$$F_{\rm adsorp} \sim n_{\rm i} c_{\rm s} \tag{3.7}$$

$$F_{\rm desorp} \sim N_{\rm s,i} \nu_{\rm vib} {\rm e}^{E_{\rm i}/kT_{\rm grain}} f_{\rm s,i} \tag{3.8}$$

where $n_{\rm i}$ is the molecular gas density and $c_{\rm s} = \sqrt{kT/\mu g}$ is the isothermal sound speed. $N_{\rm s,i} = 10^{15}$ is the number of adsorption sites per cm^2 on the grain. $\nu_{\rm vib} = 1.6 \times 10^{11} \sqrt{E_{\rm i}/\mu_{\rm i}}$ s^{-1} is the vibrational frequency of the molecules in the surface potential well, with $E_{\rm i}$ being the adsorption binding energy of the molecule in units of Kelvin. $f_{\rm s,i}$ is the fraction of occupied adsorption sites, which we take to be 1. The grain temperature $T_{\rm grain}$, is assumed to be the same temperature as the midplane temperature derived in §3.1.2. By balancing the two fluxes, we can solve for critical temperature and use it to compare with the temperature profile from §3.1.2.

These fluxes depend strongly on the species molecular properties, which are listed in table 3.2. The final calculated icelines for both passive active disks are in table 3.3 with a visual comparison between passive and active icelines for TW Hya in Figure 3.1.

Table 3.2: Species Molecular Properties (Powell et al., 2019)

Molecular Species	E_i/k [K]	$m_i \times m_H$ [g]	$n_i \times 10^{-4}$ [cm^{-3}]
H_2O	5800	18	0.9
CO_2	2000	44	0.3
CO	850	28	1.5

Table 3.3: Icelines [AU] for Passive Disks

Disk	H_2O:	passive	active	CO_2:	passive	active	CO:	passive	active
MMSN		0.12	1.81		3.36	5.94		34.0	34.2
TW Hya		0.06	2.34		1.66	7.50		16.5	21.3
HD 163296		3.28	3.39		57.9	57.9		656.5	686.5
DR Tau		0.20	2.51		5.02	8.67		56.3	56.3
CY Tau		0.19	0.95		3.48	5.00		29.2	29.9
AS 209		0.27	2.32		6.43	9.27		62.2	62.4
FT Tau		0.08	2.20		2.11	7.05		21.5	23.7
DoAr 25		0.32	1.46		5.92	7.83		50.4	51.0

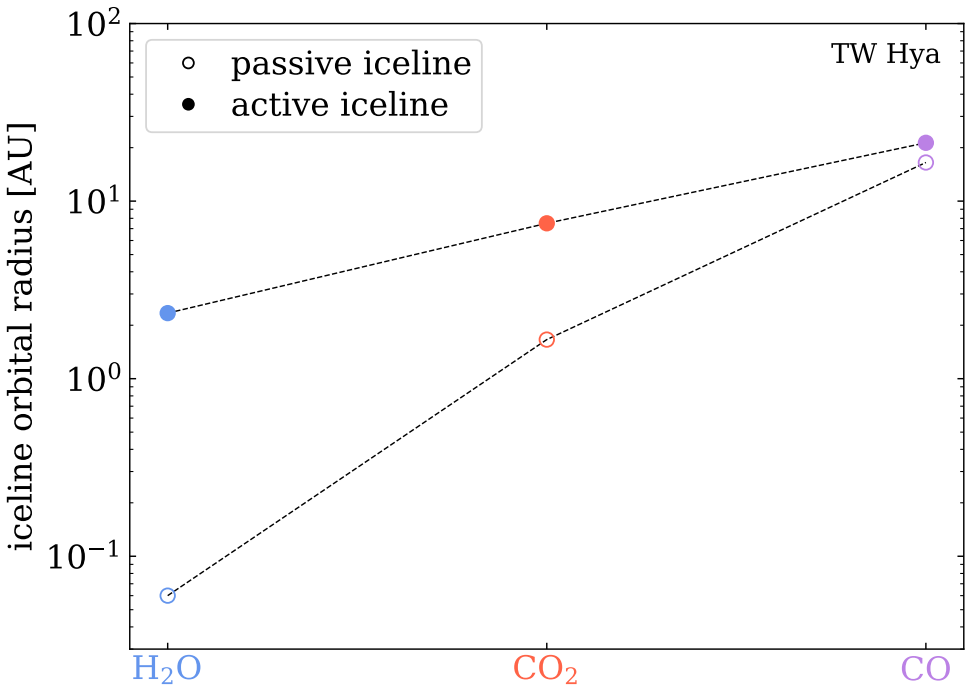

Figure 3.1: Comparison between the icelines generated for modeling TW Hya as a passive and active disk. The colors represent the molecular species, the filled circle represents an active disk including viscous heating, and the empty circle represents a passive disk without irradiation heating.

.

4

Relative Velocities of Solid Particles in Protoplanetary Disks

This chapter outlines the analytic framework of our model and specifically the calculation of where grains of different sizes will undergo collisional fragmentation. The motion of small particles in a protoplanetary disk is primarily determined by the motion of the surrounding gas and by how well the particle is coupled to the gas via gas drag. In this environment, relative velocities ($v_{\rm rel}$) between particles are typically presented in terms of each particle's dimensionless stopping time, τ, which quantifies how well-coupled the particle is to the surrounding gas over an orbital period.

Grains throughout protoplanetary disks primarily experience three different drag regimes: Epstein, Stokes, and ram pressure. Previous studies only assume the Epstein drag regime to simplify the numerical modeling of grain dynamics. When the particle size is less than the mean free path (λ) of the gas, $s \leq 9/4\lambda$, the particle experiences Epstein drag. For particles where $s \geq 9/4\lambda$, the drag regime is determined by the Reynolds number

(Re). When $Re < 1$, the particle experiences Stokes drag, and when $Re > 800$, the particle experiences ram pressure drag (Perets & Murray-Clay, 2011). We approximate particles in the intermediate Reynolds number regime by linearly extending the the Stokes and Ram pressure regimes and find the transition between the two to be where the two analytic coefficient of drag expressions intersect, ~ 54. This simple approximation deviates from the intermediate regime expression by only a marginal difference of ~ 1 (see Appendix A for derivation).

The drag forces in each regime are expressed as follows:

$$F_{\rm d} = \begin{cases} \frac{4}{3}\pi\rho_{\rm g}s^2\bar{v}_{\rm th}v_{\rm rel} & \text{Epstein} \\ 3\pi\rho_{\rm g}s\lambda\bar{v}_{\rm th}v_{\rm rel} & \text{Stokes} \\ 0.22\pi\rho_{\rm g}s^2v_{\rm rel}^2 & \text{Ram pressure} \end{cases} \tag{4.1}$$

where s is the particle radius, $\rho_{\rm g}$ is the density of the gas, $\bar{v}_{\rm th} = \sqrt{8/\pi}c_{\rm s}$ is the thermal velocity of the gas, and $v_{\rm rel}$ is the relative velocity in that regime. The particle's stopping time due to gas drag, $t_{\rm s}$, is calculated by dividing the particle's momentum, by the drag force it feels from surrounding gas (e.g. Whipple, 1972; Weidenschilling, 1977a; Chiang & Youdin, 2010; Perets & Murray-Clay, 2011).

$$t_{\rm s} = \frac{mv}{F_{\rm d}} \approx \begin{cases} \left(\frac{\rho_{\rm s}}{\rho_{\rm g}}\right)\frac{s}{\bar{v}_{\rm th}} & \text{Epstein} \\ \frac{4}{9}\left(\frac{\rho_{\rm s}}{\rho_{\rm g}}\right)\frac{s^2}{\lambda\bar{v}_{\rm th}} & \text{Stokes} \\ \left(\frac{\rho_{\rm s}}{\rho_{\rm g}}\right)\frac{s}{v_{\rm rel}} & \text{Ram} \end{cases} \tag{4.2}$$

The dimensionless stopping is then $\tau \equiv t_{\rm s}\Omega$, where Ω is the orbital angular frequency.

4.1 $\tau = 1$ Fragmentation Size

A first order approximation of where particles will break apart in a disk can be assumed by when the particles have $\tau = 1$. These marginally coupled grains will be moving at higher relative velocities and as result will probably have the most damaging collisions. By setting $\tau = 1$ and solving for the particle size for each drag regime, we obtain analytic fragmentation sizes throughout the disk. Particles that grow up to this fragmentation size, and which are growing much faster than are drifting inwards, will break at the fragmentation line. The $\tau = 1$ fragmentation line can then be made by seeing which drag regime is dominant in different regions of the disk. The inner disk is dominated by the ram pressure regime, the central disk is dominated by the Stokes regime, and the outer disk is dominated by the Epstein regime. This framework provides a good understanding of where to expect fragmentation to occur and is used to verify our robust calculation of fragmentation regions explained later on in this study. Figure 4.1 includes the $\tau = 1$ fragmentation lines for the different drag regimes and displays the approximate fragmentation line for the disk TW Hya. It also shows how the fragmentation line differs for particles of different compositions.

If we were to only assume the Epstein drag regime, the fragmentation line would be monotonically decreasing as a function of orbital radius. This creates a scenario where the particles will always be below the fragmentation line regardless of how much they have drifted inward. By including all relevant drag regimes, the fragmentation line changes creating a region in the central disk where if the particles in the outer disk are drifting faster than growing have a chance of becoming larger than the fragmentation size. Once particles are above the fragmentation size they can continue to grow unimpeded in the inner disk.

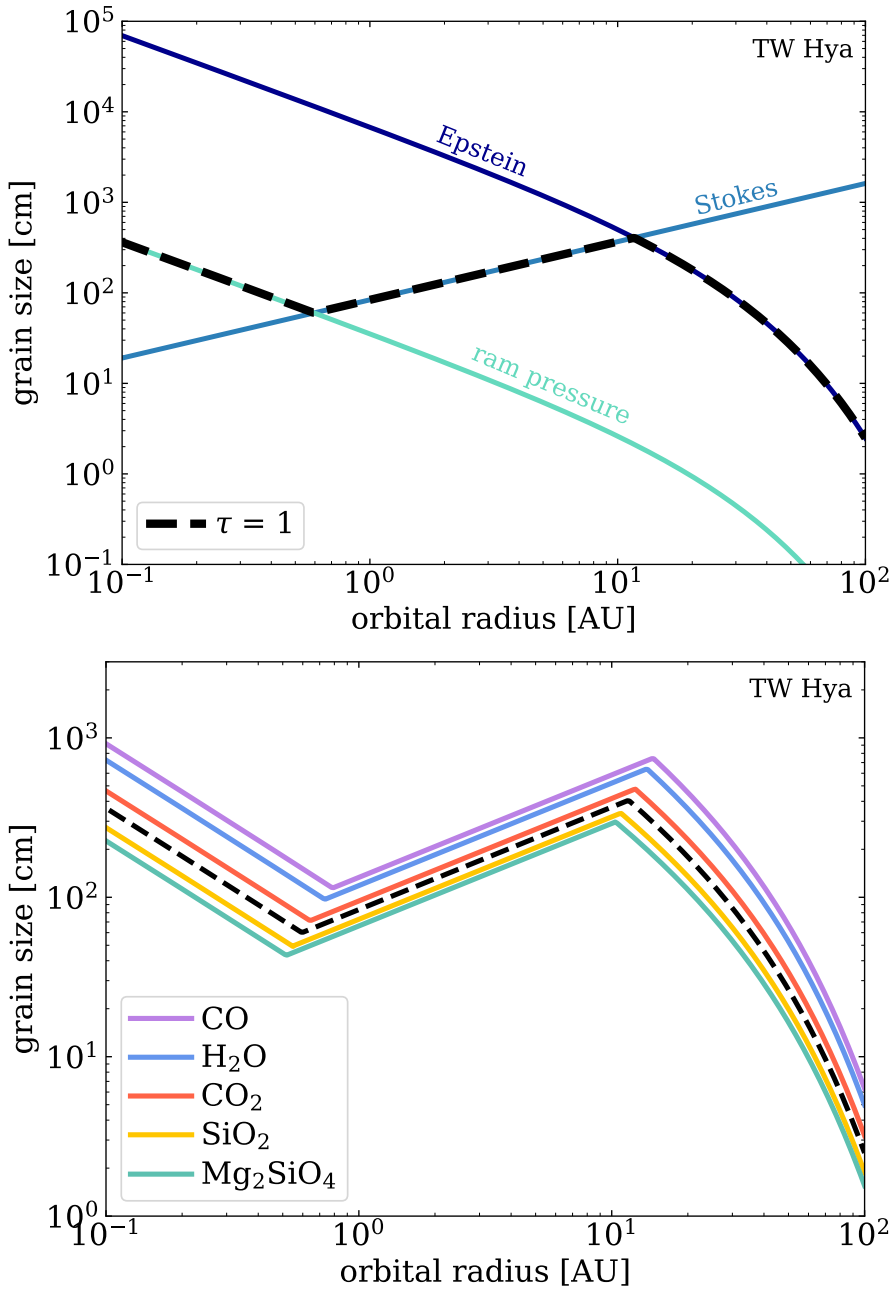

Figure 4.1: The fragmentation size profile for $\tau = 1$ particles (dashed line) throughout the disk is significantly different from previous studies when including the Epstein, Stokes, and ram pressure drag regimes (top) and varies slightly for different compositions (bottom). The dashed black profile is for a grain density of 2 g cm^{-3}, which is typically assumed. We use the disk parameters of TW Hya for both of these figures.

.

4.2 Grain Relative Velocity Derivation

A robust method of calculating regions of fragmentation throughout protoplanetary disks involves comparing the relative velocity to the critical velocities discussed in chapter 2. In this section we derive the relative velocity as function of grain size, orbital distance, disk parameters, composition, turbulence parameter, and dust-to-gas ratio. The analytic relative velocity expressions do not assume a particular grain size and do not assume a specific drag regime. The stopping time for each grain size is numerically found through an iterative process which uses its size and position in the disk to determine the relevant drag regime. Ultimately this creates a model and results that are self-consistent, which do not rely on strict assumptions and approximations.

There are two components to the relative velocity following Perets & Murray-Clay (2011): the laminar drift velocity between two grains and the grain velocity that arises due to turbulence in the disk. The laminar and turbulent velocities are derived in §4.2.1 and §4.2.2. The total relative velocity between grains will be

$$v_{\mathrm{rel,total}} = \sqrt{v_{\mathrm{laminar}}^2 + v_{\mathrm{turbulent}}^2} \tag{4.3}$$

An analysis of how various parameters affect the relative velocity is discussed in §4.3.

4.2.1 Laminar Velocity

The radial drift velocity is the relative velocity between the particle and the surrounding gas, and is most affected by the gas drag. The gas drag causes the grains to experience a head-on wind since the grains want to move Keplerian while the gas around them is moving sub-Keplerian. Thus, the laminar particle velocity involves radial and azimuthal components which incorporate the inward drift and the orbital velocity.

In laminar drift, the grains will move with velocities $v_r\hat{r} + v_\phi\hat{\phi}$, measured relative to a circular Keplerian orbit, where

$$v_r = -2\eta v_{\rm K}\left(\frac{\tau}{1+\tau^2}\right) \tag{4.4}$$

is the velocity in the radial direction, $\hat{r}$, and

$$v_\phi = -\eta v_{\rm K}\left(\frac{1}{1+\tau^2}\right) \tag{4.5}$$

is the velocity in the azimuthal direction, $\hat{\phi}$ (for a review, see Chiang & Youdin, 2010). η is the gas-pressure support parameter and can be approximated by $0.5c_s^2/v_{\rm K}^2$, where c_s is the isothermal sound speed and $v_{\rm K} = \sqrt{GM_*/r}$ is the Keplerian velocity (Weidenschilling, 1977a).

A collision between two grain particles occurs with relative velocity

$$v_{\rm laminar} = \sqrt{(v_{r,1} - v_{r,2})^2 + (v_{\phi,1} - v_{\phi,2})^2}\ , \tag{4.6}$$

where the subscripts 1 and 2 refer to evaluation of Equations (4.4) and (4.5) for particle 1 and 2, respectively.

4.2.2 Turbulent Velocity

We use the analytic framework from the appendix of Powell et al. (2019) following the full framework from Ormel & Cuzzi (2007) to calculate the relative velocity component due to gas turbulence. The turbulent relative velocity is split into three regimes based on the stopping time of both particles, $t_{\rm s1}$ and $t_{\rm s2}$ respectively, as well as the turnover time of the smallest scale eddy, $t_\eta = Re^{-0.5}t_{\rm L}$. $t_{\rm L}$ is the turnover time of the largest scale eddies, normally taken to be the local orbital period, $t_{\rm L} \sim \Omega^{-1}$.

In the *tightly coupled regime*, where $t_{\rm s1}, t_{\rm s2} < t_\eta$, particles that enter an eddy are dominated by the motion of the gas completely and realign themselves to follow the eddy. The velocity of these particles is derived by balancing the acceleration from the eddies and the acceleration from the drag.

$$v_{\rm p} = v_\eta \frac{t_{\rm s}}{t_\eta} \tag{4.7}$$

where v_η is the velocity of the smallest eddy. Then the turbulent relative velocity is simply $v_{\rm rel} = (v_\eta/t_\eta)(t_{\rm s1} - t_{\rm s2})$. This expression can be rewritten in terms of the dimensionless stopping time using the approximation $v_\eta^2 \sim v_{\rm gas}^2(t_\eta/t_{\rm L})$ as

$$v_{\rm turbulent}^2 = v_{\rm gas}^2 \frac{t_{\rm L}}{t_\eta}(\tau_{\rm s1} - \tau_{\rm s2})^2 \tag{4.8}$$

with $v_{\rm gas} = \sqrt{\alpha c_s^2}$ as the gas velocity. Particles in the tightly coupled regime are mostly expected in the outer disk and will primarily be affected by the Epstein drag law.

In the *intermediately coupled regime*, the larger particle can be marginally coupled to some of the eddies, with $t_\eta < t_{\rm s} < t_{\rm L}$. The majority of particles in a protoplanetary disk are expected to be in the intermediately coupled regime and are dominated by the Stokes and Epstein drag laws. While both particles are still well-coupled to the largest scale eddy, they have low velocities. If a particle decouples from the eddy, the relative velocity follows the total eddy velocity. In this case the relative velocity only depends on the dimensionless stopping time of the largest particle, and the full expression of the turbulent relative velocity from Ormel & Cuzzi (2007) is

$$v_{\rm turbulent}^2 = v_{\rm gas}^2 \left[2y_{\rm a} - (1+\epsilon) + \frac{2}{1+\epsilon}\left(\frac{1}{1+y_{\rm a}} + \frac{\epsilon^3}{y_{\rm a}+\epsilon}\right)\right]\tau_{\rm s} \tag{4.9}$$

where $y_{\rm a} = 1.6$ and $\epsilon = \tau_{\rm s1}/\tau_{\rm s2}$. This expression can be generalized to a simple analytic

expression

$$v^2_{\text{turbulent}} = C v^2_{\text{gas}} \tau \tag{4.10}$$

where C is ~ 3 for different sized particles and ~ 2 for same sized particles.

In the *heavy particle regime*, $\tau \gg 1$, the largest scale eddies randomly interact with the motion of the particle causing slight random walk perturbations in the particles velocity. These large heavy particles are typically found in the inner disk and only experience the ram pressure drag law. The RMS relative turbulent velocity is given by $\langle \delta v^2 \rangle = \langle \delta v_1^2 \rangle + \langle \delta v_2^2 \rangle - 2\langle \delta v_1 \delta v_2 \rangle$, with the RMS velocity of each particle given as $v = v_{\text{gas}}/\sqrt{1+\tau}$. While smaller particles will interact and have a non-zero $\langle \delta v_1 \delta v_2 \rangle$, these heavy particles will have $\langle \delta v_1 \delta v_2 \rangle = 0$. Plugging in the RMS velocity of each particles gives a relative RMS turbulent velocity of

$$\langle \delta v^2 \rangle = v^2_{\text{gas}} \left(\frac{1}{1+\tau_{\text{s1}}} + \frac{1}{1+\tau_{\text{s2}}} \right) = v^2_{\text{turbulent}} \tag{4.11}$$

The iterative solving of the stopping time regime allows us to not assume a turbulent relative velocity equation and thus follows whichever turbulent velocity regime the grain will experience.

4.3 Relative Velocity Analysis

The total relative velocity derived above is used to explore a large parameter space. It depends on which disk is modeled, how porous the grains are, the composition of the grain, how turbulent the environment is, and the size ratio between the two colliding particles. It is also inherently a function of both the size and orbital distance of the grain. Understanding how this parameter space changes the relative velocity throughout a disk is crucial to mod-

eling accurate fragmentation regions in both size and distance. The turbulence parameter , α, the size ratio, f, and the porosity, ϕ, have the most influence on the relative velocity.

The level of turbulence determines the speed of the gas and for all marginally coupled particles means that the larger the turbulence, the larger the relative velocity. Increasing the turbulence is important for sizes studied in this analysis since the larger the relative velocity the easier it is for a collision to result in fragmentation. Figure 4.2 compares the relative velocity as a function of grain size and orbital radius of 3 different α's: 10^{-2}, 10^{-3}, and 10^{-4}. These values are typically used for modeling protoplanetary dusty fluid environments.

The particle size ratio is an important parameter in terms of the relative velocity because the level of fragmentation and relevance strongly depend on the size of the target grain and the location in the disk. Figure 4.3 looks at how the relative velocity changes for different size ratios and grain sizes at 3 different locations in the disk, 1, 10, and 100 AU. At intermediate sizes, the size ratio is not important, however at very small and large sizes there is a significant difference throughout the disk. By increasing the size ratio, the relative velocity decreases, making those collisions less destructive, but it is important to note that with higher mass particles the overall collision energy is higher.

Porosity of the grain is a proxy for how many bonds hold the grain together. The more bonds there are, the stronger the grain. Figure 4.4 calculates the relative velocity as before but for varying level of porosity. The least porous grains have lower relative velocities making them less susceptible to fragmentation.

The choices we make for these variables will be detailed in chapter 6.

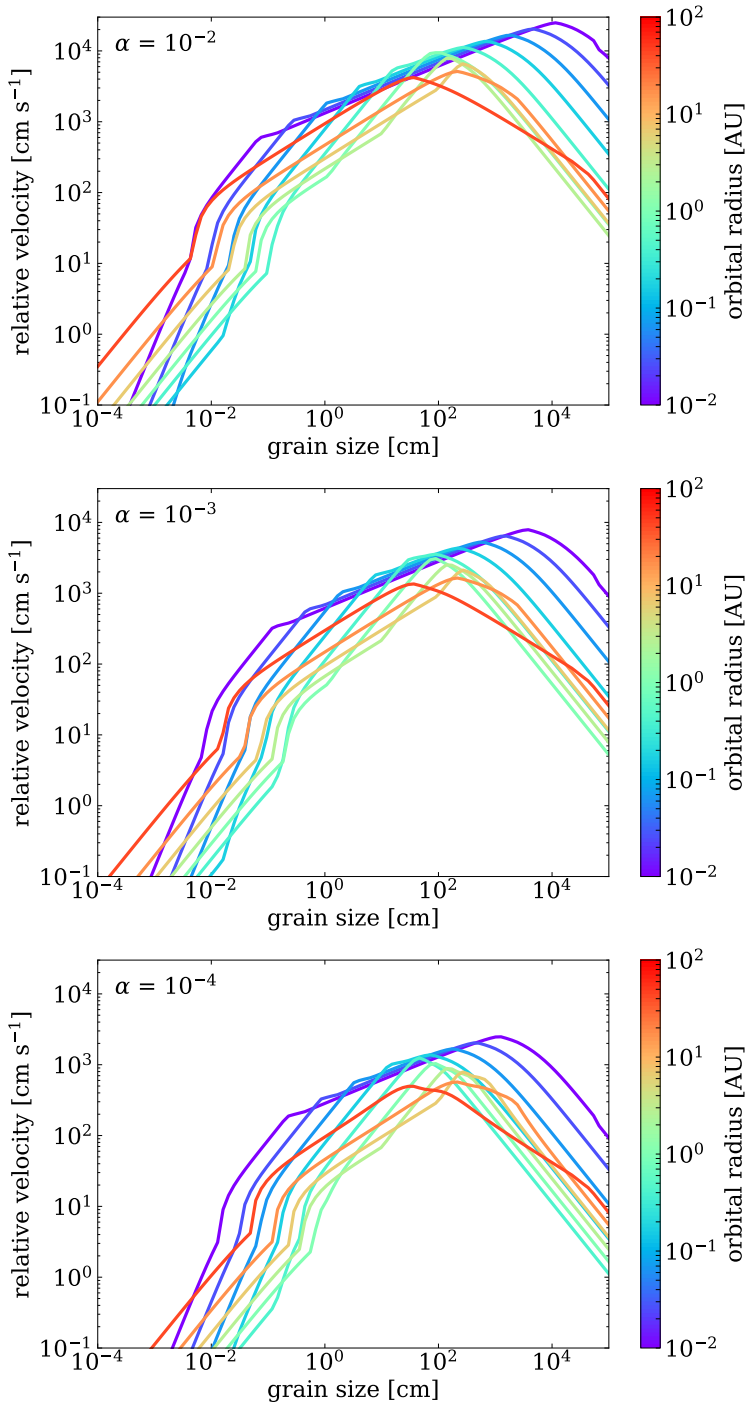

Figure 4.2: Relative velocities for a general composition in TW Hya for varying grain sizes, orbital radii, and turbulence. The collisions modeled are for a projectile grain that is half the size of the target grain. In order from top to bottom is for α of 10^{-2}, 10^{-3}, and 10^{-4}.

.

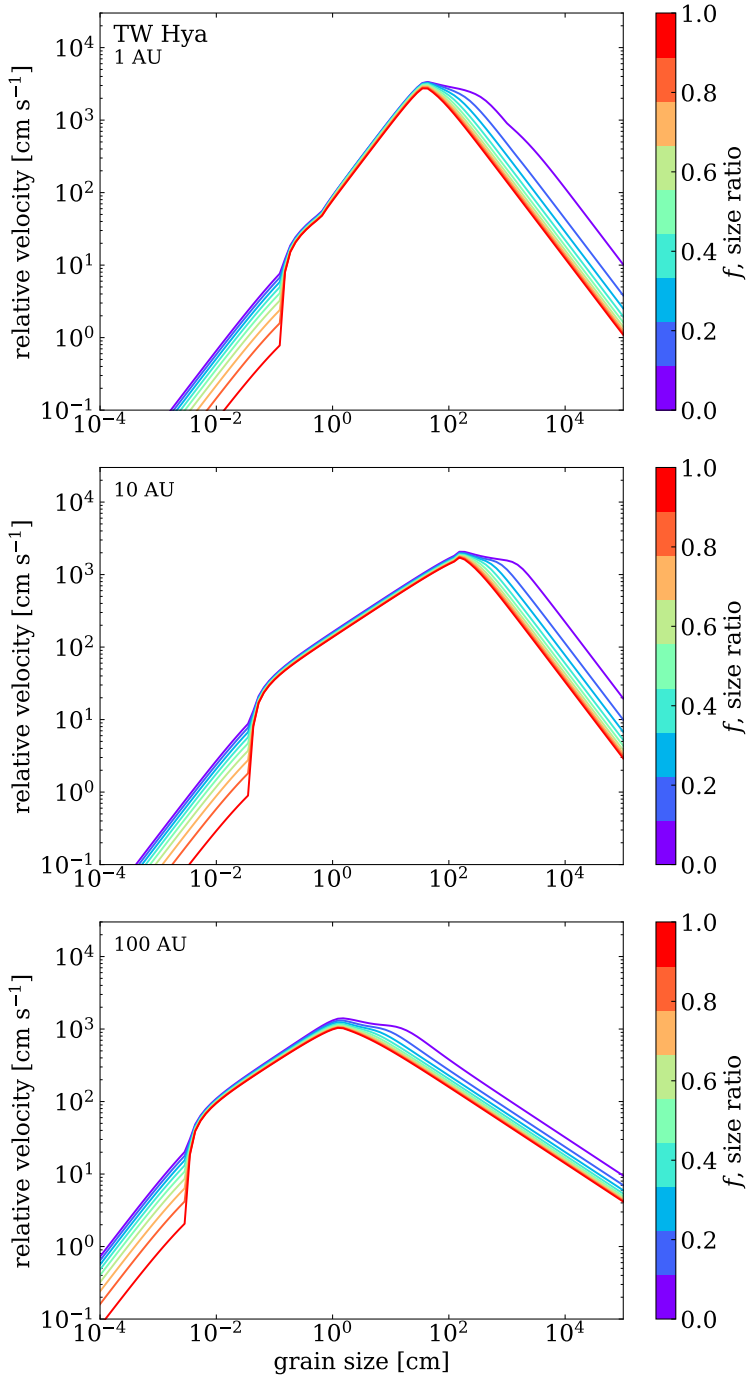

Figure 4.3: Relative velocities for a general composition in TW Hya with $\alpha = 10^{-3}$ for varying grain sizes, orbital radii, and grain size ratios. In order from top to bottom is for an orbital distance of 1, 10, and 100 AU.

.

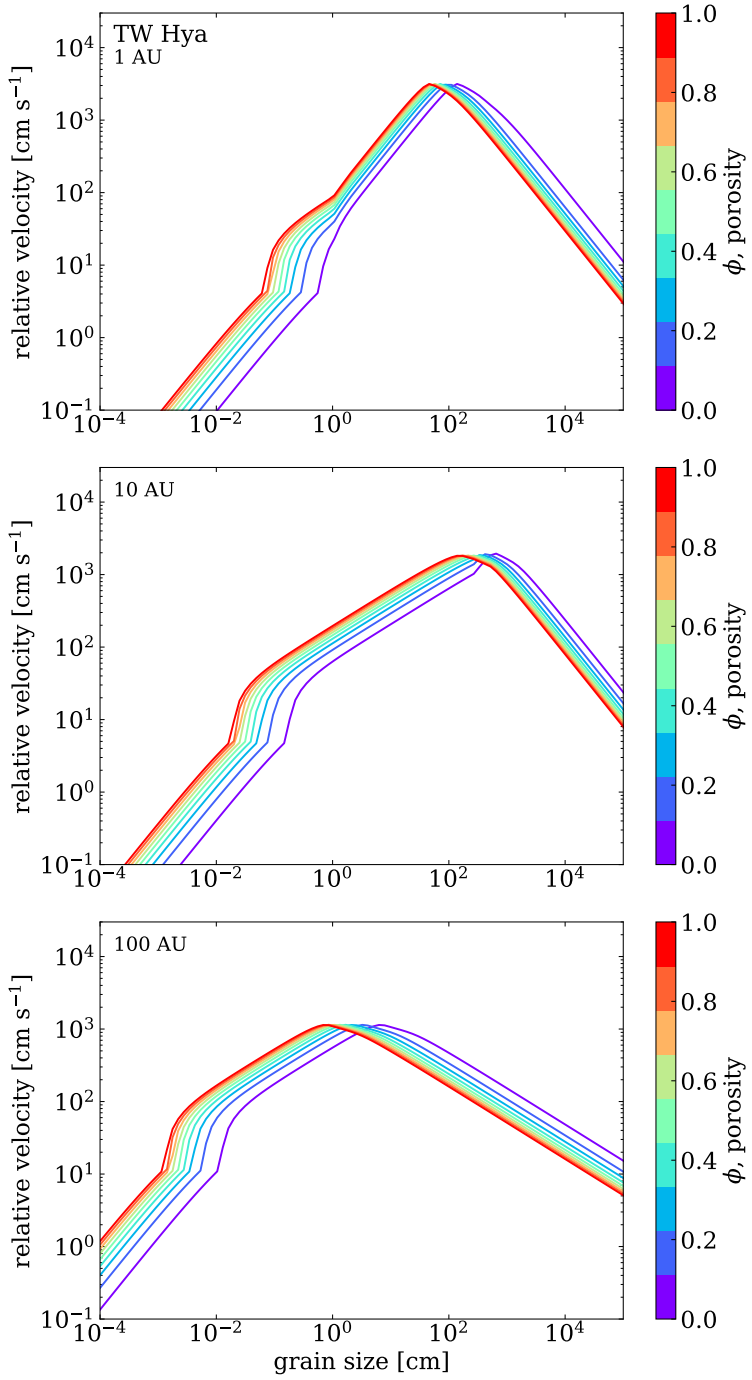

Figure 4.4: Relative velocities for a general composition in TW Hya with $\alpha = 10^{-3}$ for grain sizes, orbital radii, and level of porosity. In order from top to bottom is for an orbital distance of 1, 10, and 100 AU.

.

5

Growth & Drift Timescales

We use the grain growth and drift timescales to compare whether grains throughout the disk are either growing faster or slower than they are drifting inwards. When grains are growth dominant they are much more susceptible to fragmentation. In the simple $\tau = 1$ fragmentation line case, all particles throughout the disk that are growing will fragment once they reach the fragmentation size if they are growing much faster than they are drifting. However, if they are drifting much faster than growing, they have a higher chance of surviving fragmentation as they drift and grow above the fragmentation size. To visualize which timescale dominates, we find where the growth timescale equals to the drift timescale as a function of grain size and orbital distance. The growth and drift timescales are derived in §5.1 and §5.2 respectively following Armitage (2017).

5.1 Growth Timescale

The growth timescale, how quickly particles grow from submillimeter to meter sizes through collisions, is defined as $\tau_g = m/\dot{m}$, where m is the mass of the grain, and $\dot{m}$ is the

collisional growth rate.

$$m = \frac{4}{3}\pi\rho_{\rm int}s^3 \tag{5.1}$$

$$\dot{m} = \rho_{\rm d}\sigma\Delta v \tag{5.2}$$

s is the radius of the particle and $\rho_{\rm int}$ is the internal density of the particle depending on composition. $\rho_d = f_{\rm d}\rho_{\rm g}$ is the volumetric denisty of the particles in the disk, where $f_{\rm d}$ is the ratio of the gas surface density and the dust surface density, and $\rho_{\rm g}$ is the the density of the gas. $\sigma = \pi s^2$ is the cross sectional area of the particle and $v_{\rm rel}$ is the relative velocity between the particles.

Simplifying to the terms mentioned above,

$$\tau_{\rm g} = \frac{4}{3}\frac{\rho_{\rm int}s}{f_{\rm d}\rho_{\rm g}v_{\rm rel}}. \tag{5.3}$$

We assume that the the particles perfectly stick together when they collide with other like-sized particles as long as the relative velocity does not surpass the critical velocity. This assumption is substantial for the analytic model (Blum & Wurm, 2008).

5.2 Drift Timescale

The drift timescale gives a time for how quickly these particles drift inwards. The outward pressure gradiant of the gas in the protoplanetary disk coupled with the force of drag these particles feel due to the sub-Keplerian gas causes these particles to lose angular momentum and radially drift inwards. The timescale is then $\tau_d = |r/\dot{r}|$, where r is the

orbital radius and $\dot{r}$ is the the radial drift velocity. The radial drift velocity is the same as the relative laminar drift radial velocity from 4.

$$\dot{r} \approx -2\eta\Omega r \left(\frac{\tau}{1+\tau^2}\right) \tag{5.4}$$

$\eta = 0.5c_s^2/v_k^2$ is the gas-pressure support parameter, where c_s is the isothermal sound speed and v_k the Keplerian velocity (Weidenschilling, 1977a).

The drift timescales is then simplified to

$$\tau_{\rm d} = (2\eta\Omega)^{-1}\left(\frac{1+\tau^2}{\tau}\right) \tag{5.5}$$

The drift velocity is the fastest when $s \sim 1$ meter, and $\tau_{\rm d}$ becomes too short for particles to grow to large sizes (Chiang & Youdin, 2010).

5.3 Timescale Analysis

The growth and drift timescales, derived in sections 5.1 and 5.2, play an important role in understanding which regions of the disk contribute to rapid growth or an inward flux of dust. Regions where growth and drift timescales are the same is sensitive to which disk is modeled since the surface densities are different. The surface density profile changes the orbital radius at which the growth timescale equals to the drift timescale. For the MMSN and for a 1 meter particle, the switch from $\tau_{\rm g} < \tau_{\rm d}$ to $\tau_{\rm g} > \tau_{\rm d}$ occurs at a few AU. For the larger disks, the switch occurs at around 10 AU. This means that the particle spends more time growing in a larger disk then it does for the MMSN. The size of the particle and the dust-to-gas ratio also affect where $\tau_{\rm g} = \tau_{\rm d}$. Figure 5.1 compares the timescales for the MMSN and TW Hya for particles of 1 and 100 cm sizes.

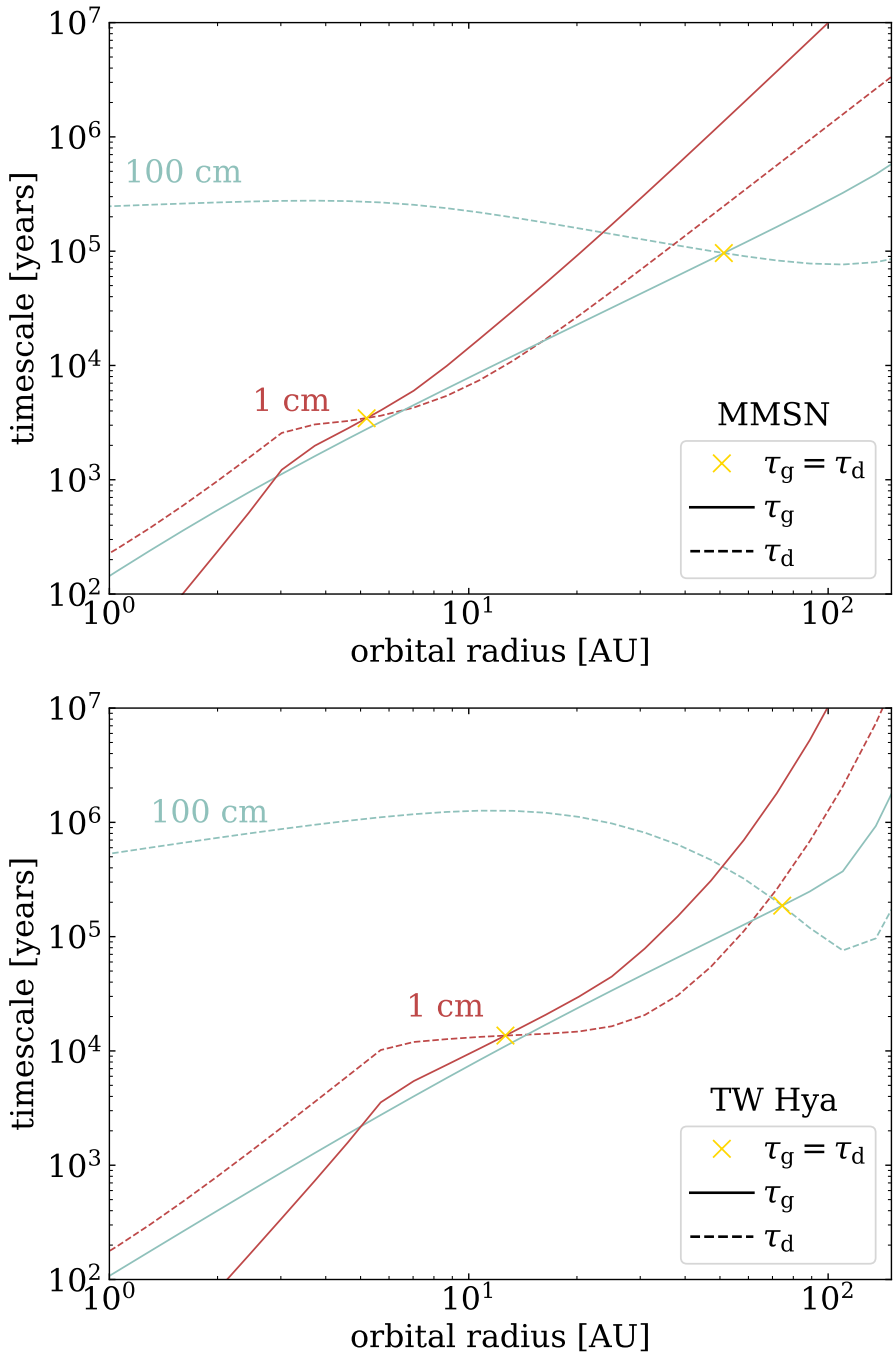

Figure 5.1: Growth and drift timescale comparison for 1 and 100 cm-sized particles for TW Hya. The red lines are for the 1cm-size particle and the light blue lines are for the 100cm-size particle. The grains have an internal density of 2 g cm^{-3}. Dashed lines are drift timescales and solid line are growth timescales.

.

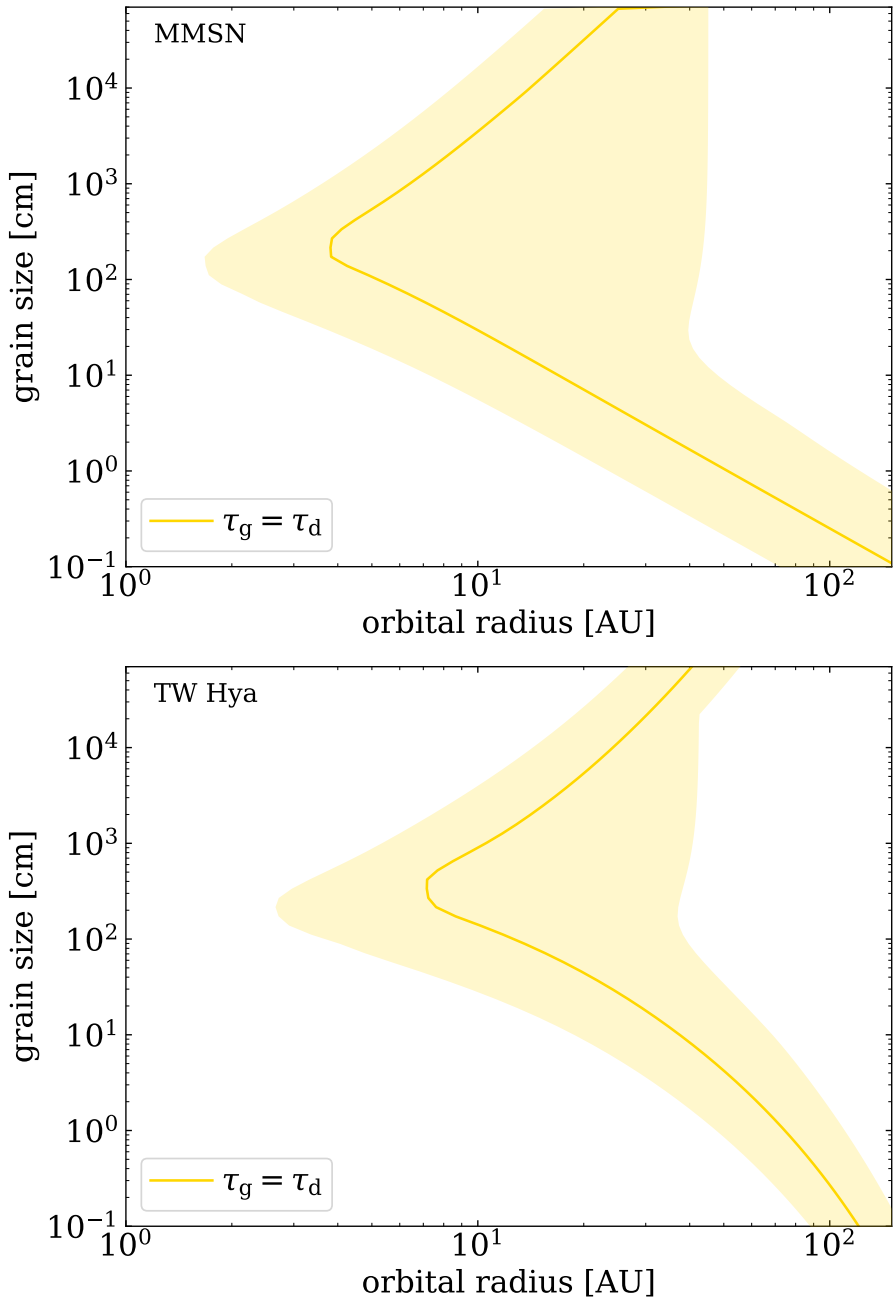

Figure 5.2: Continuous $\tau_g = \tau_d$ regions spanning a dust-to-gas ratio of 10^{-4} - 10^{-2} for the MMSN and TW Hya. The central line represents a dust-to-gas ratio of 10^{-3}. The left of the $f_d = 10^{-3}$ $\tau_g = \tau_d$ line is growth dominated and everything to right is drift dominated. For all dust-to-gas ratios tested, the grains in the inner disk are always growing faster than they are drifting and the grains in the outer disk are always drifting inward faster than they are growing.

.

6

Fiducial Parameters & Results

In order to model millimeter- to meter-sized grain dynamics and relative velocities in protoplanetary disks, several fiducial parameters must be set. In terms of grains, for all of the calculations we assume that the collisions between two particles occurs for a target particle with a projectile particle that is not the same size as the target particle. Specifically, our model defines the projectile radius as $r_{\rm p} = f r_{\rm t}$ where $r_{\rm t}$ is the target radius, and the size-ratio throughout the entire model is then $f \equiv r_{\rm p}/r_{\rm t}$. The size ratio is set at initialization of the model run and is propagated through the calculations of the dimensionless stopping time τ, relative velocity $v_{\rm rel}$, and timescales $\tau_{\rm d}$ & $\tau_{\rm g}$. We choose $f = 0.5$ since the majority of collisions between particles at a specific semi-major axis will not occur with the same sized particle. Instead, half the size is a reasonable intermediate size that provides the most information about fragmentation and growth. The size ratio does change the relative velocity slightly (fig. 4.3). The second grain parameter we set is the porosity. Grains of this size are not massive enough to compress themselves from their own self-gravity, and they cannot differentiate their interiors as protoplanets ($\sim$100km) do. Thus, they are most likely

“fluffier" or more porous than the small rocks we see on the surface of the Earth. We set a filling factor at the initialization of the model run that also propagates through all the calculations by making the total grain density $\rho_{\rm g} = \phi\rho_{\rm i}$, where $\rho_{\rm i}$ is the material density (table 2.2) and ϕ is the porosity. We take $\phi = 0.3$, which translates to 70% of the grain being empty. The more porous the grain is, the weaker it is, making the grain more susceptible to fragmentation (fig. 4.4) and is a more accurate portrayal of protoplanetary disk dusty grain strengths. The ice coating however, would not be porous. When modeling an aggregate grain, we assume that the monomer size is 0.1μm as discussed in §2.3. For the disk, the fiducial parameters are the dust-to-gas density ratio and the turbulence level α. We use a dust-to-gas ratio of 10^{-3}, which is a mid-range value typically assumed in protoplanetary disks with 10^{-2} as the maximum and 10^{-5} as the minimum. Turbulence in protoplanetary disks should vary throughout the entire disk, however a simplistic value of $\alpha = 10^{-3}$ can be used to model the turbulence's first-order effects. α typically varies from 10^{-4} - 10^{-2} in active disks (fig. 4.2), and is assumed to be 0 for laminar disks.

We calculate collisional fragmentation regions, where particles of a certain size are expected to break, depending on their composition. Grain particles will fragment if their relative velocity $v_{\rm rel}$, in the disk reaches the critical fragmentation velocities $v_{\rm crit}$. By equating the relative velocity to the critical velocities (derived in chapter 2), we can solve for the size and orbital radius of fragmentation. We do so by using `SciPy's` optimization package with `fsolve`, a numerical root-finding function for non-linear equations. Due to the shape of the relative velocity as a function of grain size and orbital radius, there are two sizes for each orbital radius where $v_{\rm rel} = v_{\rm crit}$ as long as $v_{\rm rel} > v_{\rm crit}$. The difference between the two fragmentation sizes tapers to one size as the relative velocity for each orbital radius

approaches $v_{\rm rel} < v_{\rm crit}$. This method of calculating fragmentation regions is much more robust as compared to the $\tau = 1$ fragmentation size from §4.1. This method does not rely on assuming that $\tau = 1$, and instead solves for the corresponding τ depending on the grain size and position in disk. Other than the fiducial parameters discussed above, we do not make any other assumptions about the dynamics.

6.1 Rocky Fragmentation Region

We present fragmentation regions that best represent rocks with no ice coverage using the critical velocity description provided by Stewart & Leinhardt (2009) from §2.1. Figures 6.1 and 6.2 are the calculated fragmentation regions for the passive and active disks of the MMSN and TW Hya respectively. Porous rock is significantly weaker than strong rock with fragmentation regions spanning throughout the entire disk and spanning many orders of magnitude in grain size. Solid rock, however, has much smaller fragmentation regions —specifically in passive and active disks fragmentation only occurs in the outer disk and affects a small range of grain sizes. Both regions follow the $\tau = 1$ fragmentation profile defined by the different drag regimes. The MMSN has a larger span of fragmentation sizes in the outer disk than TW Hya.

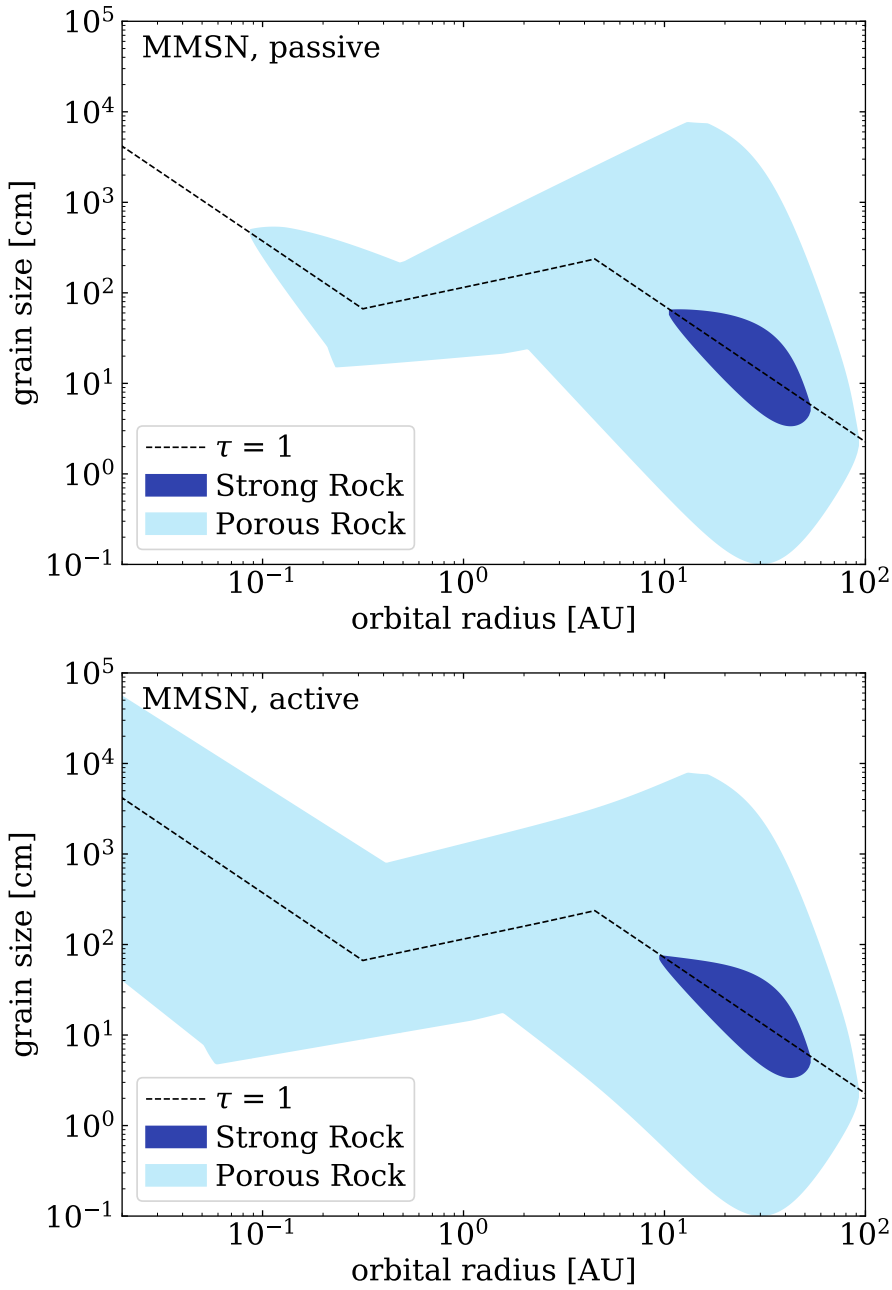

Figure 6.1: Fragmentation regions found using the critical velocity prescription defined in Stewart & Leinhardt (2009) from §2.1 for the MMSN. The light blue region is for weak, porous rock, and the dark blue region is for strong rock. The top figure uses a passive disk temperature profile, and the bottom figure uses an active disk temperature profile. $\tau = 1$ fragmentation line (§4.1) included for comparison.

.

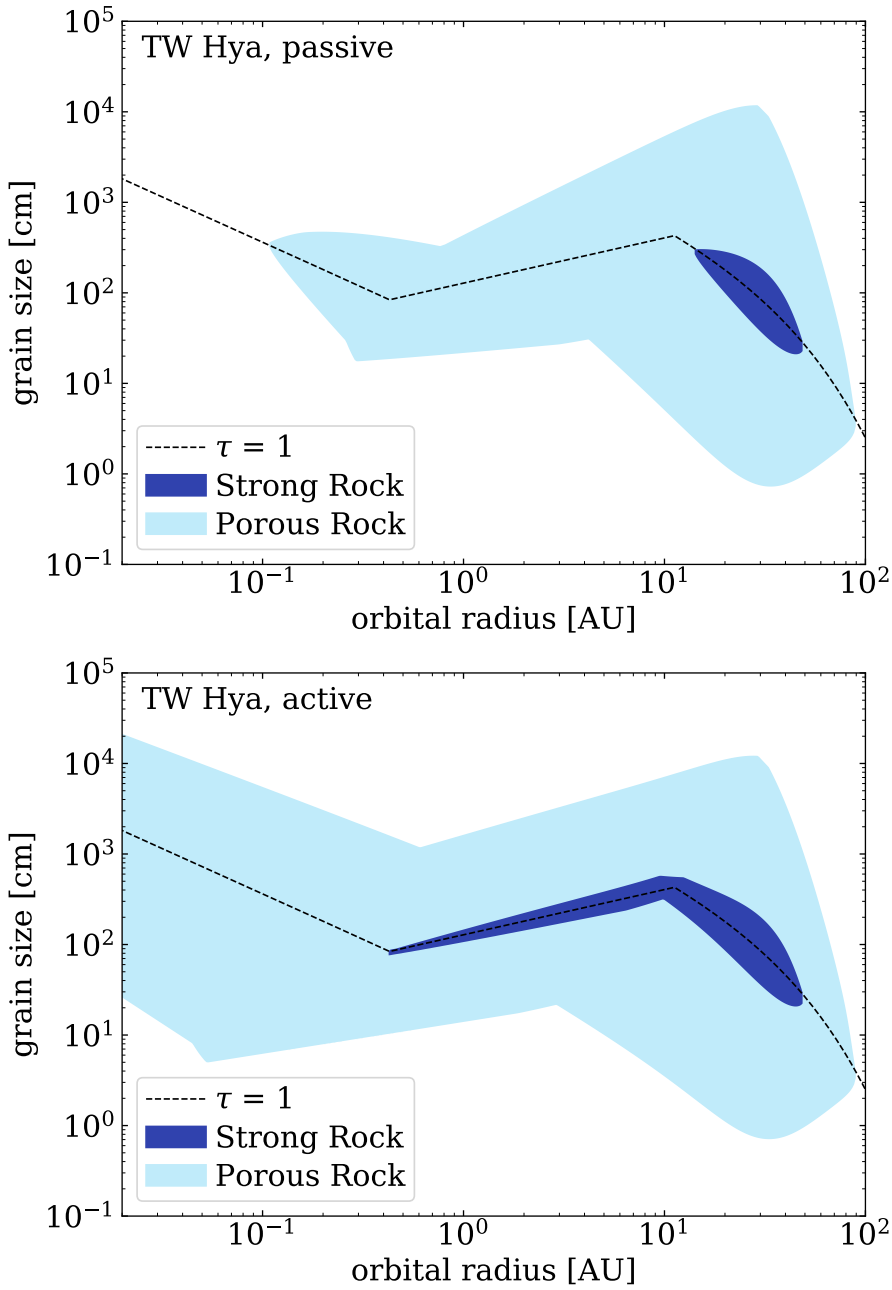

Figure 6.2: Fragmentation regions found using the critical velocity prescription defined in Stewart & Leinhardt (2009) from §2.1 for TW Hya. Same as figure 6.1, only modeling TW Hya.

.

6.2 Icy Fragmentation Region

We present fragmentation regions that best represent rocks with ice coverage using the critical velocity description provided by Wada et al. (2007, 2009) with updated material property values from §2.2. Figures 6.3 and 6.4 are the calculated fragmentation regions for the MMSN with passive and active heating respectively. Figures 6.5 and 6.6 are the calculated fragmentation regions for TW Hya with passive and active heating respectively. Compact BPCA grains coated by CO_2 ice (red), CO ice (purple), and H_2O ice (blue) in the outer disk dominate the fragmentation process and elucidate a path were collisional destruction does not play a significant role on grain growth throughout the majority of the disk. Regions of grain fragmentation strongly depend on the monomer composition, relative position to the various icelines (dashed lines), compactness of the aggregate (denoted by BCCA or BPCA), and whether there is active heating in the disk. The left and right columns shows fragmentation of BCCA and BPCA particles respectively. The top rows has the fully calculated regions excluding effects of icelines on the grains. The bottom rows take into account desorption of ices interior to the icelines and considers the case where freeze out of volatile species is expected to coat rocky silicate grains, such as SiO_2 (yellow) and Mg_2SiO_4 (green). The black solid line is where the growth and drift timescales are equivalent (chapter 5). The fragmentation regions are fairly similar between the MMSN and TW Hya. The main results of using the Wada et al. (2007, 2009) critical velocity with relevant icelines (bottom rows of figures 6.3-6.6), is that where there are no colorful fragmentation regions, there is no collisional fragmentation. Particles that are in a non-colored region of the grain size - orbital radius parameter space can grow without a fragmentation barrier.

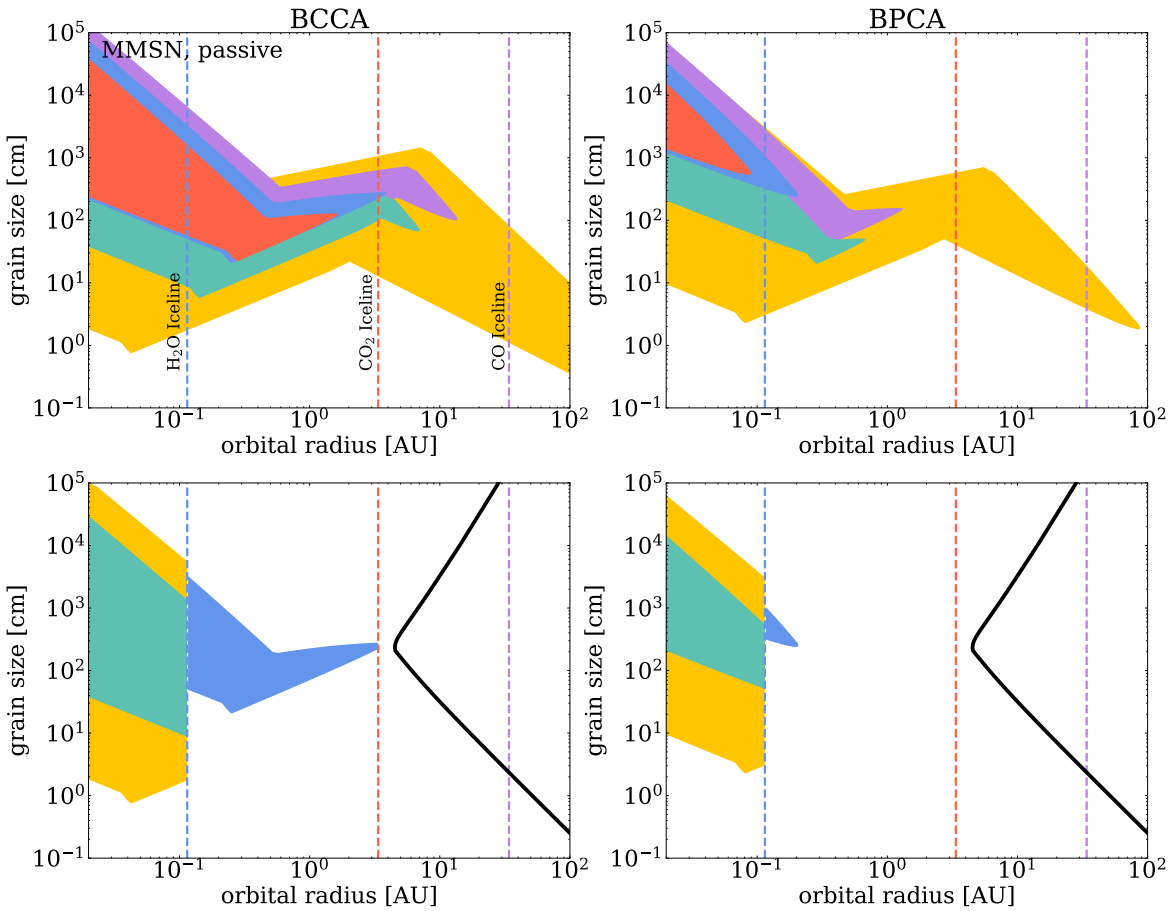

Figure 6.3: Fragmentation regions found using the critical velocity prescription defined in Wada et al. (2007, 2009) from §2.2 for the MMSN with passive heating. The materials are represented by their respective colors which are consistent with previous plots: SiO_2 (yellow), Mg_2SiO_4 (green), H_2O (blue), CO_2 (red), and CO (purple). The dashed colored lines are the compositional icelines with matching colors. The bottom row considers desorption of ices at each respective iceline. The black line is where $\tau_g = \tau_d$. The left column is for BCCA (fluffy aggregates), and the right column is for BPCA (compact aggregates).

.

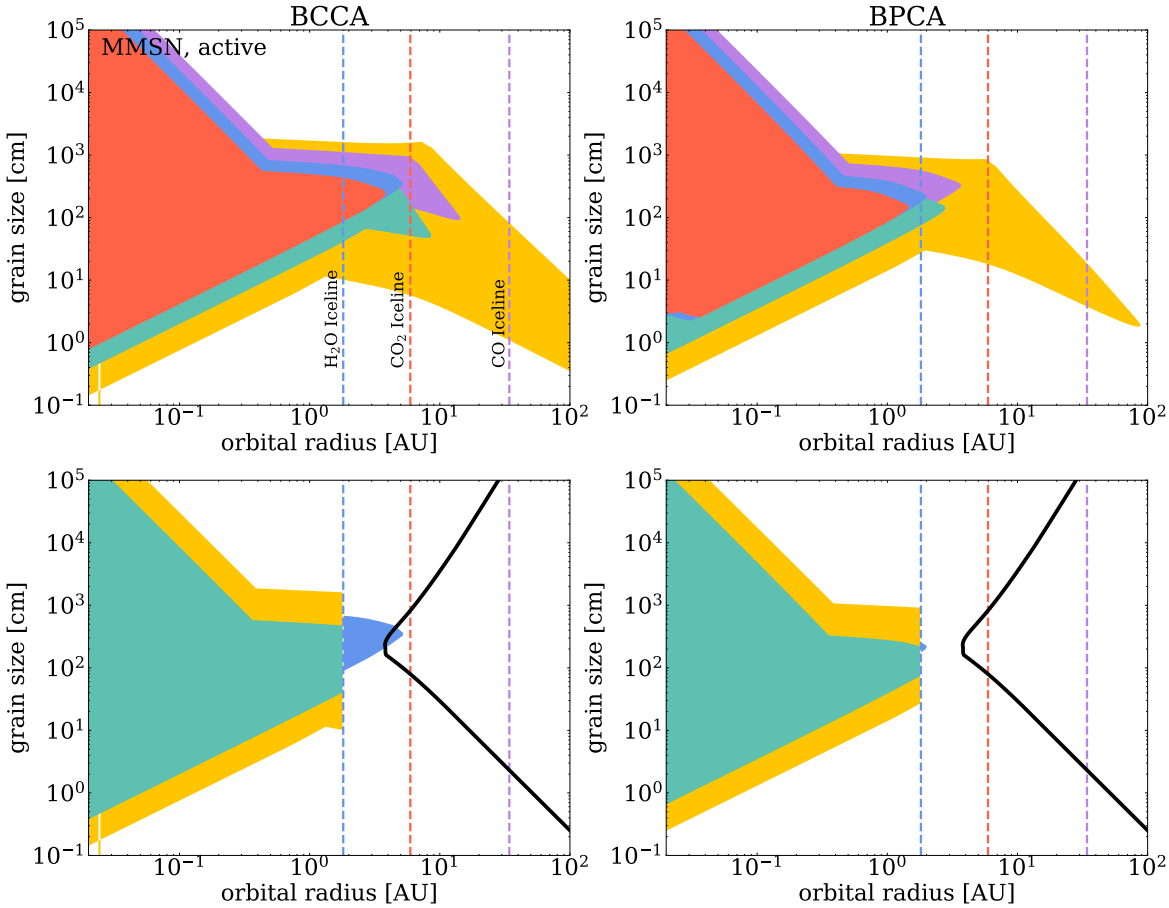

Figure 6.4: Fragmentation regions found using the critical velocity prescription defined in Wada et al. (2007, 2009) from §2.2 for the MMSN with active heating. Same as technical description in Figure 6.3.

.

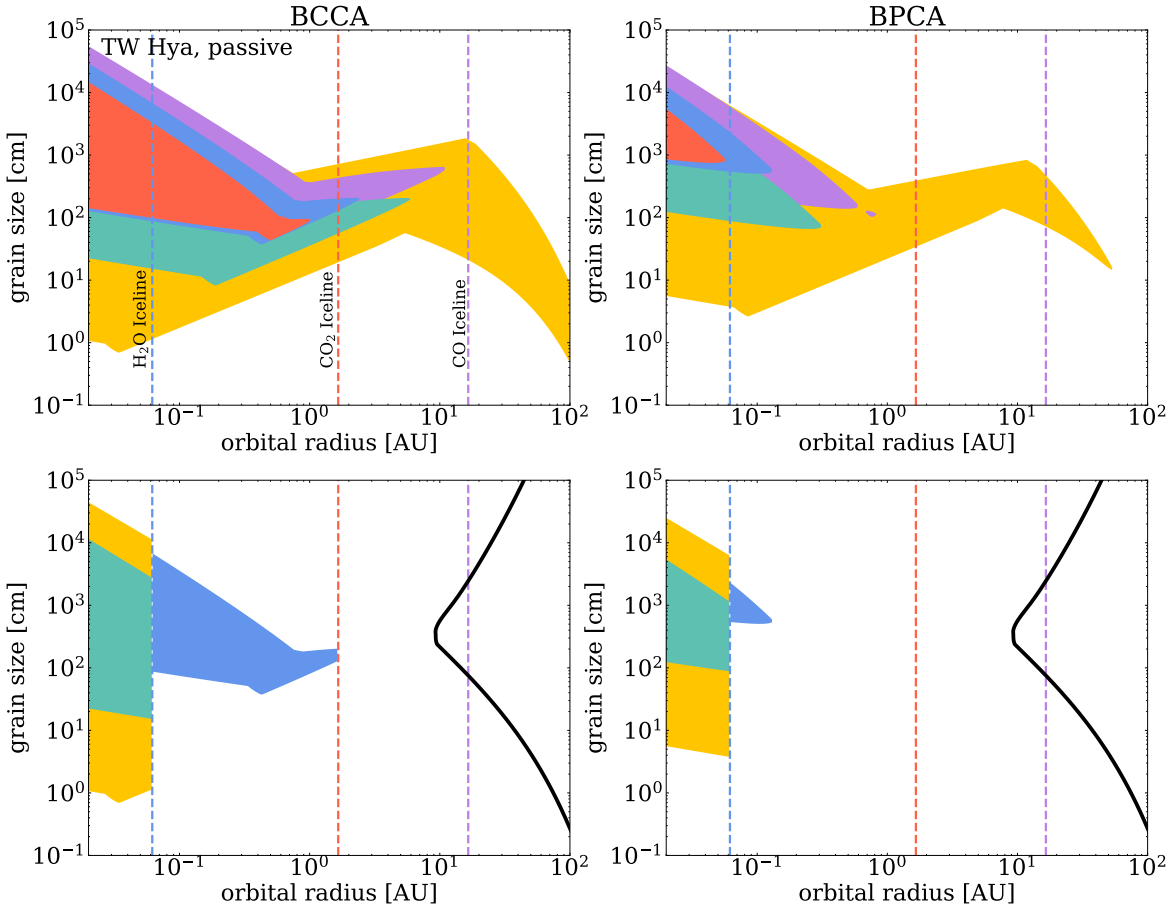

Figure 6.5: Fragmentation regions found using the critical velocity prescription defined in Wada et al. (2007, 2009) from §2.2 for TW Hya with passive heating. Same as technical description in Figure 6.3.

.

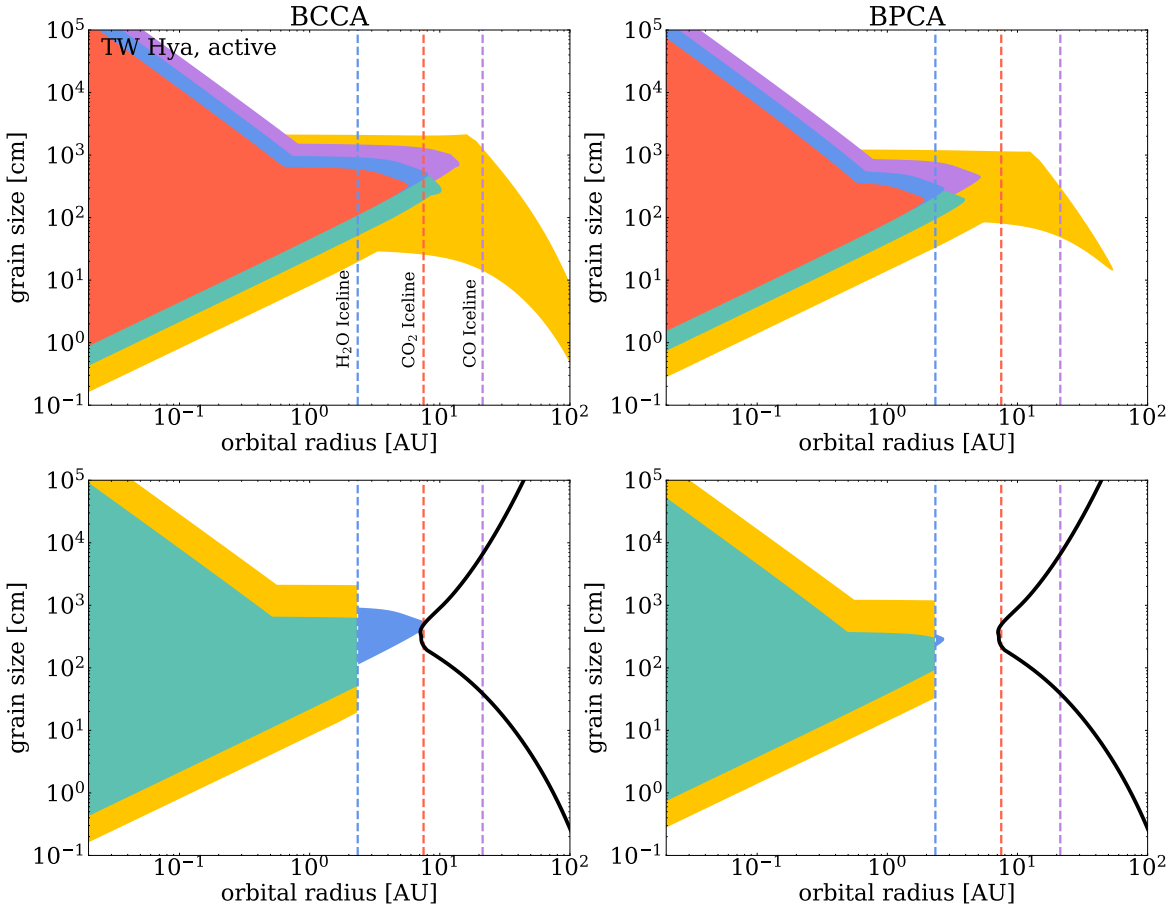

Figure 6.6: Fragmentation regions found using the critical velocity prescription defined in Wada et al. (2007, 2009) from §2.2 for TW Hya with active heating. Same as technical description in Figure 6.3.

.

7

Discussion & Summary

This thesis outlines an updated understanding and modeling of protoplanetary disk grain fragmentation. The model presented removes strict assumptions about the grains themselves, including their compositions and dynamics, as well as outdated assumptions of protoplanetary disk surface densities. Our semi-analytic model explicitly calculates particle relative velocities depending on where a particle of a certain size is in the disk. We are able to initialize the model with the particles composition, size-ratio with a colliding particle, and porosity, and the disk with a dust-to-gas ratio, α turbulence parameter, and whether the disk is heated with only stellar irradiation or with accretion heating as well. The model does not assume that the particles are marginally or well-coupled to the gas ($\tau \leq 1$), and instead solves for the corresponding τ depending on the particles size and orbital radius. By including all relevant drag regimes—Epstein, Stokes, and ram pressure—we are able to accurately calculate τ for all grain sizes throughout the entire disk. This model allows us to study growth, drift, and fragmentation for an extremely broad parameter space in protoplanetary disks. This work also updates and recalculates critical fragmentation

velocities from two different studies (Stewart & Leinhardt, 2009; Wada et al., 2007, 2009) with recent experimental calculations of material properties and assumptions about material strengths.

The result of the model are outputs of fragmentation regions which span orders of magnitude in grain size and orbital radius, that depend on grain and disk properties. The outer bounds of these regions are determined by where the relative velocity reaches the critical fragmentation velocity. Result plots in chapter 6, present colorful fragmentation regions of the critical velocity calculations. Particles that are in these regions will break apart from any collision that occurs with a particle that is at least half its size. The different shapes of the fragmentation regions are caused by the relevant drag force, strength and composition of the grain, and the heating throughout the disk.

Fragmentation regions calculated using the critical velocity derived from Stewart & Leinhardt (2009) (§2.1) demonstrate that porous rocky grains will break apart from any collision throughout the entire active disk in both the MMSN and TW Hya cases. Grain growth above the meter-size is not possible via collisional growth for these porous rocky bodies, as the light blue fragmentation regions of figures 6.1-6.2 spans 4 orders of magnitude in size and nearly 3 orders of magnitude in orbital radius. For strong rocks, however, the fragmentation region decreases substantially. The dark blue fragmentation regions for strong rock in figures 6.1-6.2 is confined to the outer disk and only spans 1 order of magnitude in grain size. Although collisional growth is possible for these strong grains, the strong rock material properties are somewhat outdated from Housen & Holsapple (1990, 1999) and are best used for strength-dominated large bodies such as asteroids. Thus, it may be more accurate to use compositional strengths of silicates to model rocky grains or perform further

experimental work on strength-dominated smaller bodies.

Fragmentation regions calculated using the critical velocity derived from Wada et al. (2007, 2009) (§2.2) for various compositions have very different shapes from the Stewart & Leinhardt (2009) fragmentation regions. Although, for all the different cases the regions do follow the $\tau = 1$ simple analytic fragmentation line. In this case, fragmentation regions strongly depend on composition. Fluffy BCCA aggregates are also much weaker than compact BPCA aggregates. We believe that BPCA aggregates are much more common in protoplanetary disks than BCCA aggregates since collisions tend to compact fluffy aggregates.

SiO_2: Silica (denoted by the yellow regions in figures 6.3-6.6) is the weakest material and easily undergoes fragmentation for a broad range of sizes throughout the entire disk assuming it is not coated by any ices. All silica grains will undergo collisional fragmentation, and cannot explain planetesimal growth via collisional growth.

CO_2: Carbon dioxide ice (denoted by the red regions in figures 6.3-6.6) is the strongest material modeled and does not easily fragment. Fragmentation for most CO_2 grain sizes will occurs within a few AU where the temperature of the disk is too hot for CO_2 ice to actually exist. In fact, when including desorption of ices, the CO_2 fragmentation region is well interior to the corresponding CO_2 iceline and as a result CO_2 ice grains and silicates covered in CO_2 ice beyond the CO_2 iceline will survive all collisions. This means that carbon dioxide does not undergo collisional fragmentation in protoplanetary disks.

Mg_2SiO_4, H_2O, and CO: Forsterite, water ice, and carbon monoxide ice (denoted by the green, blue, and purple regions respectively in figures 6.3-6.6) are all relatively the same strength and have similar fragmentation regions. Their fragmentation regions effect

larger-sized aggregates in the inner to mid disk. Forsterite is stronger than silica but still has a large spanning region of fragmentation. However, forsterite grains do not undergo collisional fragmentation in the outer disk and have the potential to grow via collisions. In observed disks, such as TW Hya, BPCA forsterite aggregates beyond 1 AU will survive all collisions. A similar analysis from carbon dioxide ice can be applied to water and carbon monoxide ices. All grains interior to their respective icelines will evaporate. Since carbon monoxide ice fragmentation is interior to its iceline, all carbon monoxide ice collisions will survive beyond its iceline. Similarly, only a small fraction of water ice grains will actually undergo collisional fragmentation beyond the water iceline.

By incorporating accurate relative velocity calculations and iceline physics, we determine that ice grains and silicate grains covered in ice are resilient to collisions in the outer disk. All ice grains in the very outer disk will quickly drift inwards until they begin growing as quickly as they are drifting. This is the black curve in figures 6.3-6.6. Once particles reach $\tau_{\rm g} = \tau_{\rm d}$, they will follow the profile until they reach the leftmost peak of $\tau_{\rm g} = \tau_{\rm d}$. From that point, growth becomes much faster than drift and all grains unaffected by collisional fragmentation (those that do not fall within any colored fragmentation region) will continue to grow unimpeded where eventually other growth mechanisms for gravity-dominated bodies will proceed. Larger disks provide a much longer time for grains in the outer disk to drift and grow, and is the reason behind TW Hya's fragmentation regions being smaller than the MMSN fragmentation regions. Accretion heating in disks pushes the icelines further out in the disk causing much larger inner disk fragmentation regions than in passive disks.

The next progression of this work will be to analyze the other disks mentioned in

table 3.1 and compare their fragmentation regions to the nominal MMSN and TW Hya. Specifically, understanding how the fragmentation regions corresponded with even more massive disks, such as AS 209, will be instrumental in figuring out whether the initial amount of formation material in disks is important for the outcomes of planet formation. Secondly, we will model the time evolution of these grains in order to quantitatively answer whether outer disk grains can drift and undergo collisional growth through the disk.

In conclusion, this work finds that:

1. Collisional fragmentation of millimeter-meter size grains strongly depends on the material properties. While silicates tend to undergo collisional fragmentation throughout the entire disk, some ices in the outer disk never reach critical fragmentation velocities and do not experience fragmentation in disks.

2. Compact aggregates composed of 0.1 micron monomers are much stronger than porous solid rocks and fluffier aggregates.

3. Lastly, the total disk mass, i.e. the disk surface density, may be an important initial condition which sets the timescales for inward drift, collisional growth, and collisional fragmentation.

Bibliography

Armitage, P. J. (2017). Physical processes in protoplanetary disks. *arXiv:1509.06382 [astro-ph]*.

Bergin, E. A., Cleeves, L. I., Gorti, U., Zhang, K., Blake, G. A., Green, J. D., Andrews, S. M., Evans Ii, N. J., Henning, T., Öberg, K., Pontoppidan, K., Qi, C., Salyk, C., & van Dishoeck, E. F. (2013). An old disk still capable of forming a planetary system. *Nature*, 493(7434), 644–646.

Birnstiel, T., Klahr, H., & Ercolano, B. (2012). A simple model for the evolution of the dust population in protoplanetary disks. *Astronomy and Astrophysics*, 539, A148.

Blum, J. & Münch, M. (1993). Experimental investigations on aggregate-aggregate collisions in the early solar nebula. *Icarus*, 106, 151.

Blum, J. & Schräpler, R. (2004). Structure and Mechanical Properties of High-Porosity Macroscopic Agglomerates Formed by Random Ballistic Deposition. *Physical Review Letters*, 93, 115503.

Blum, J., Schräpler, R., Davidsson, B. J. R., & Trigo-Rodríguez, J. M. (2006). The Physics

of Protoplanetesimal Dust Agglomerates. I. Mechanical Properties and Relations to Primitive Bodies in the Solar System. *The Astrophysical Journal*, 652, 1768–1781.

Blum, J. & Wurm, G. (2000). Experiments on Sticking, Restructuring, and Fragmentation of Preplanetary Dust Aggregates. *Icarus*, 143, 138–146.

Blum, J. & Wurm, G. (2008). The Growth Mechanisms of Macroscopic Bodies in Protoplanetary Disks. *Annual Review of Astronomy and Astrophysics*, 46(1), 21–56.

Blum, J., Wurm, G., Kempf, S., Poppe, T., Klahr, H., Kozasa, T., Rott, M., Henning, T., Dorschner, J., Schräpler, R., Keller, H. U., Markiewicz, W. J., Mann, I., Gustafson, B. A., Giovane, F., Neuhaus, D., Fechtig, H., Grün, E., Feuerbacher, B., Kochan, H., Ratke, L., El Goresy, A., Morfill, G., Weidenschilling, S. J., Schwehm, G., Metzler, K., & Ip, W.-H. (2000). Growth and Form of Planetary Seedlings: Results from a Microgravity Aggregation Experiment. *Physical Review Letters*, 85, 2426–2429.

Blum, J., Wurm, G., Poppe, T., & Heim, L.-O. (1998). Aspects of Laboratory Dust Aggregation with Relevance to the Formation of Planetesimals. *Earth Moon and Planets*, 80, 285–309.

Blum, J., Wurm, G., Poppe, T., Kempf, S., & Kozasa, T. (2002). First results from the cosmic dust aggregation experiment codag. *Advances in Space Research*, 29, 497–503.

Brown, P. P. & Lawler, D. F. (2003). Sphere Drag and Settling Velocity Revisited. *Journal of Environmental Engineering*, 129(3), 222–231.

Cheng, N.-S. (2009). Comparison of formulas for drag coefficient and settling velocity of spherical particles. *Powder Technology*, 189(3), 395–398.

Chiang, E. & Laughlin, G. (2013). The minimum-mass extrasolar nebula: In situ formation of close-in super-Earths. *Monthly Notices of the Royal Astronomical Society*, 431(4), 3444–3455.

Chiang, E. & Youdin, A. (2010). Forming Planetesimals in Solar and Extrasolar Nebulae. *Annual Review of Earth and Planetary Sciences*, 38(1), 493–522.

Dominik, C. & Tielens, A. G. G. M. (1997). The Physics of Dust Coagulation and the Structure of Dust Aggregates in Space. *The Astrophysical Journal*, 480, 647–673.

Gaillac, R., Pullumbi, P., & Coudert, F.-X. (2016). ELATE: An open-source online application for analysis and visualization of elastic tensors. *Journal of Physics: Condensed Matter*, 28(27), 275201.

Goldreich, P. & Ward, W. R. (1973). The Formation of Planetesimals. *The Astrophysical Journal*, 183, 1051.

Hartmann, L., Calvet, N., Gullbring, E., & D'Alessio, P. (1998). Accretion and the Evolution of T Tauri Disks. *The Astrophysical Journal*, 495, 385–400.

Hayashi, C. (1981). Structure of the Solar Nebula, Growth and Decay of Magnetic Fields and Effects of Magnetic and Turbulent Viscosities on the Nebula. *Progress of Theoretical Physics Supplement*, 70, 35–53.

Hollenbach, D., Kaufman, M. J., Bergin, E. A., & Melnick, G. J. (2008). WATER, O2, AND ICE IN MOLECULAR CLOUDS. *The Astrophysical Journal*, 690(2), 1497–1521.

Housen, K. R. & Holsapple, K. A. (1990). On the fragmentation of asteroids and planetary satellites. *Icarus*, 84(1), 226–253.

Housen, K. R. & Holsapple, K. A. (1999). Scale Effects in Strength-Dominated Collisions of Rocky Asteroids. *Icarus*, 142(1), 21–33.

Johansen, A., Klahr, H., & Henning, T. (2006). Gravoturbulent Formation of Planetesimals. *The Astrophysical Journal*, 636(2), 1121.

Kataoka, A., Tanaka, H., Okuzumi, S., & Wada, K. (2013). Fluffy dust forms icy planetesimals by static compression. *Astronomy & Astrophysics*, 557, L4.

Kozasa, T., Hasegawa, H., & Nomoto, K. (1989). Formation of dust grains in the ejecta of SN 1987A. *The Astrophysical Journal*, 344, 325–331.

Krause, M. & Blum, J. (2004). Growth and Form of Planetary Seedlings: Results from a Sounding Rocket Microgravity Aggregation Experiment. *Physical Review Letters*, 93, 021103.

Langkowski, D., Teiser, J., & Blum, J. (2008). The Physics of Protoplanetesimal Dust Agglomerates. II. Low-Velocity Collision Properties. *The Astrophysical Journal*, 675, 764–776.

Lynden-Bell, D. & Pringle, J. E. (1974). The evolution of viscous discs and the origin of the nebular variables. *Monthly Notices of the Royal Astronomical Society*, 168, 603–637.

Mazzoldi, A., Hill, T., & Colls, J. J. (2008). CFD and Gaussian atmospheric dispersion models: A comparison for leak from carbon dioxide transportation and storage facilities. *Atmospheric Environment*, 42, 8046–8054.

Musiolik, G. & Wurm, G. (2019). Contacts of Water Ice in Protoplanetary Disks - Laboratory Experiments. *The Astrophysical Journal*, 873(1), 58.

Öberg, K. I., Murray-Clay, R., & Bergin, E. A. (2011). The Effects of Snowlines on C/O in Planetary Atmospheres. *The Astrophysical Journal Letters*, 743, L16.

Ormel, C. W. & Cuzzi, J. N. (2007). Closed-form expressions for particle relative velocities induced by turbulence. *Astronomy & Astrophysics*, 466(2), 413–420.

Paraskov, G. B., Wurm, G., & Krauss, O. (2007). Impacts into weak dust targets under microgravity and the formation of planetesimals. *Icarus*, 191, 779–789.

Perets, H. B. & Murray-Clay, R. A. (2011). Wind-shearing in gaseous protoplanetary disks and the evolution of binary planetesimals. *The Astrophysical Journal*, 733(1), 56.

Pollack, J. B., Hubickyj, O., Bodenheimer, P., Lissauer, J. J., Podolak, M., & Greenzweig, Y. (1996). Formation of the Giant Planets by Concurrent Accretion of Solids and Gas. *Icarus*, 124(1), 62.

Powell, D., Murray-Clay, R., Pérez, L. M., Schlichting, H. E., & Rosenthal, M. (2019). New Constraints From Dust Lines On The Surface Densities Of Protoplanetary Disks. *The Astrophysical Journal*, 878(2), 116.

Powell, D., Murray-Clay, R., & Schlichting, H. E. (2017). Using Ice and Dust Lines to Constrain the Surface Densities of Protoplanetary Disks. *The Astrophysical Journal*, 840(2), 93.

Schäfer, C., Speith, R., & Kley, W. (2007). Collisions between equal-sized ice grain agglomerates. *Astronomy and Astrophysics*, 470, 733–739.

Shivamurthy, A., S, P., R, P. G., M, R. N., & J, S. R. (2019). Study of surface energy of SiO2 and TiO2 on charge carrier mobility of rubrene organic field effect transistor.

In *THE 3rd INTERNATIONAL CONFERENCE ON THEORETICAL AND APPLIED NANOSCIENCE AND NANOTECHNOLOGY.*

Simon, J. B., Armitage, P. J., Li, R., & Youdin, A. N. (2016). THE MASS AND SIZE DISTRIBUTION OF PLANETESIMALS FORMED BY THE STREAMING INSTABILITY. I. THE ROLE OF SELF-GRAVITY. *The Astrophysical Journal*, 822(1), 55.

Sprow, F. B. & Prausnitz, J. M. (1966). Vapor-Liquid equilibria for five cryogenic mixtures. *AIChE Journal*, 12(4), 780–784.

Squire, J. & Hopkins, P. F. (2018). Resonant Drag Instabilities in protoplanetary disks: The streaming instability and new, faster-growing instabilities. *Monthly Notices of the Royal Astronomical Society*, 477(4), 5011–5040.

Stewart, S. T. & Leinhardt, Z. M. (2009). VELOCITY-DEPENDENT CATASTROPHIC DISRUPTION CRITERIA FOR PLANETESIMALS. *The Astrophysical Journal*, 691(2), L133–L137.

Vorobyov, E. I. (2011). Embedded Protostellar Disks Around (Sub-)Solar Stars. II. Disk Masses, Sizes, Densities, Temperatures, and the Planet Formation Perspective. *The Astrophysical Journal*, 729(2), 146.

Wada, K., Tanaka, H., Suyama, T., Kimura, H., & Yamamoto, T. (2007). Numerical Simulation of Dust Aggregate Collisions. I. Compression and Disruption of Two-Dimensional Aggregates. *The Astrophysical Journal*, 661(1), 320–333.

Wada, K., Tanaka, H., Suyama, T., Kimura, H., & Yamamoto, T. (2009). COLLISIONAL

GROWTH CONDITIONS FOR DUST AGGREGATES. *The Astrophysical Journal*, 702(2), 1490–1501.

Weidenschilling, S. J. (1977a). Aerodynamics of solid bodies in the solar nebula. *Monthly Notices of the Royal Astronomical Society*, 180(2), 57–70.

Weidenschilling, S. J. (1977b). The Distribution of Mass in the Planetary System and Solar Nebula. *Astrophysics and Space Science*, 51(1), 153.

Whipple, F. L. (1972). On certain aerodynamic processes for asteroids and comets. In *From Plasma to Planet* (pp. 211).

Wurm, G. & Blum, J. (1998). Experiments on Preplanetary Dust Aggregation. *Icarus*, 132, 125–136.

Wurm, G., Paraskov, G., & Krauss, O. (2005). Ejection of dust by elastic waves in collisions between millimeter- and centimeter-sized dust aggregates at 16.5 to 37.5 m/s impact velocities. *Physical Review E*, 71, 021304.

Youdin, A. N. (2004). Obstacles to the Collisional Growth of Planetesimals. *Star Formation in the Interstellar Medium: In Honor of David Hollenbach*, 323, 319.

Youdin, A. N. & Goodman, J. (2005). Streaming Instabilities in Protoplanetary Disks. *The Astrophysical Journal*, 620(1), 459–469.

Youdin, A. N. & Shu, F. H. (2002). Planetesimal Formation by Gravitational Instability. *The Astrophysical Journal*, 580(1), 494–505.

Appendix A

Deriving the Reynolds number for Distinguishing Between the Stokes and Ram Pressure Drag Regimes

The Intermediate drag regime is set for particles which have a Reynolds number of $1 < \mathrm{Re} < 800$ spanning in between the Stokes and ram pressure regime, and for the full range of Reynolds numbers the drag regime is

$$F_{\mathrm{D}} = 0.5 C_{\mathrm{D}} \pi r^2 \rho_{\mathrm{g}} v_{\mathrm{rel}}^2 \tag{A.1}$$

where C_{D} is the coefficient of drag which is a function of the Reynolds number (Brown & Lawler, 2003; Cheng, 2009; Perets & Murray-Clay, 2011). For $10^{-3} < Re < 10^5$, C_{D} is

$$C_{\mathrm{D}} = \frac{24}{\mathrm{Re}} \left(1 + 0.27\mathrm{Re}\right)^{0.43} + 0.47 \left[1 - \exp\left(-0.44\mathrm{Re}^{0.38}\right)\right]. \tag{A.2}$$

We determine the difference between the intermediate drag regime to the Stokes and ram pressure regimes by comparing C_{D} of the three different regimes. C_{D} for the Stokes

and ram pressure regimes are found by equating the relevant drag force equation (eq. 4.1) to the general drag force equation (eq. A.1), and solving for C_{D}. Figure A.1 demonstrates the comparison between the coefficients of drag. We find that by approximating the Reynolds number switch for going between the Stokes regime and ram pressure regime to be where they intersect, at Re $\approx$ 54.1, it only differs from the analytic C_{D} equation by a factor of 1.08. Not modeling the intermediate regime fully does not change this works results.

$$C_{\mathrm{D,Stokes}} = 24/\mathrm{Re} \tag{A.3}$$

$$C_{\mathrm{D,Ram}} = 0.44 \tag{A.4}$$

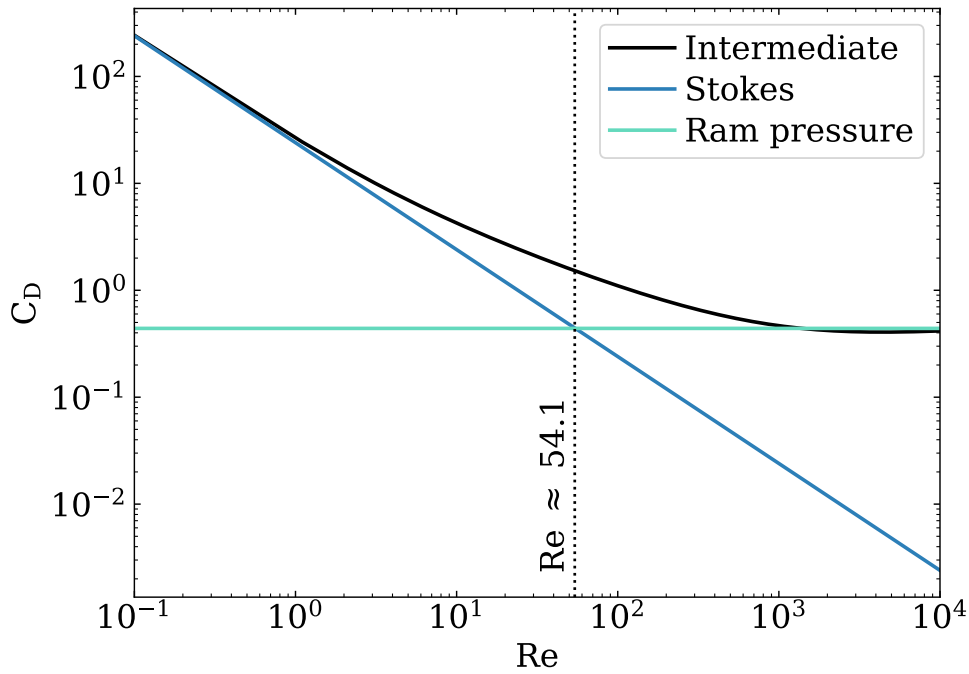

Figure A.1: Comparison of the analytic expressions of the coefficients of drag C_{D} for the intermediate, Stokes, and ram pressure drag laws. The vertical dotted line is the switch between Stokes and ram pressure regimes, and is found to be at Re $\approx$ 54.1. The separation between the Stokes and ram pressure intersection point with the intermediate curve at Re $\approx$ 54.1 is 1.08.

.